Accepted Manuscript

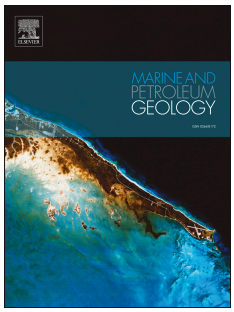

Evolution of porosity and pore types in organic-rich, calcareous, Lower Toarcian Posidonia Shale

Eliza J. Mathia, Leon Bowen, K. Mark Thomas, Andrew C. Aplin

PII: S0264-8172(16)30104-0

DOI: 10.1016/j.marpetgeo.2016.04.009

Reference: JMPG 2527

To appear in: *Marine and Petroleum Geology*

Received Date: 3 February 2016

Revised Date: 10 April 2016

Accepted Date: 11 April 2016

Please cite this article as: Mathia, E.J., Bowen, L., Thomas, K.M., Aplin, A.C., Evolution of porosity and pore types in organic-rich, calcareous, Lower Toarcian Posidonia Shale, *Marine and Petroleum Geology* (2016), doi: 10.1016/j.marpetgeo.2016.04.009.

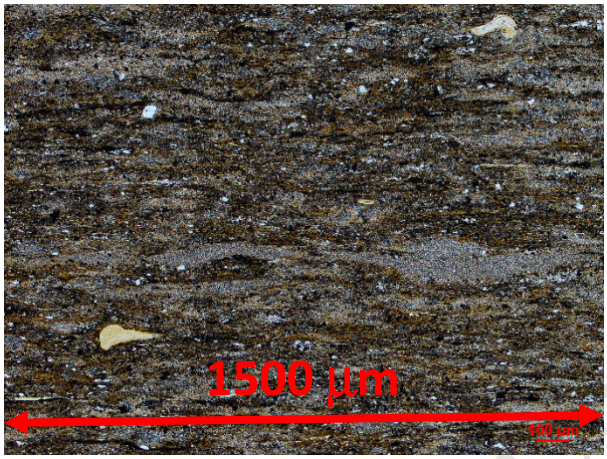

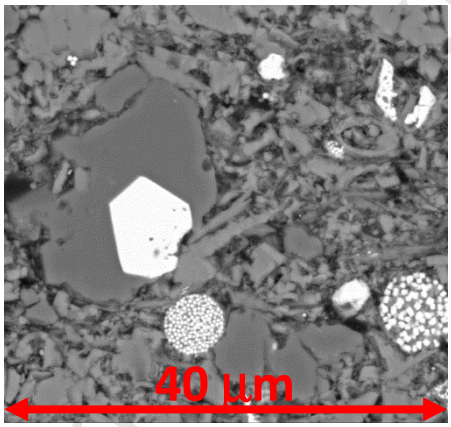

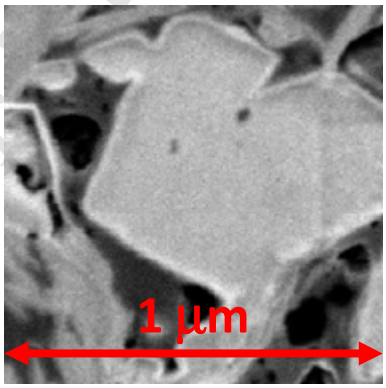

Evolution of Porosity and Pore Types in Organic-rich, Calcareous, Lower Toarcian Posidonia Shale

Eliza J. Mathia[1,5,*], Leon Bowen[2], K. Mark Thomas[3], Andrew C. Aplin[4,*]

[1]School of Civil Engineering and Geosciences, Newcastle University, Newcastle upon Tyne, NE1 7RU, United Kingdom

[2]Department of Physics, Durham University, Science Laboratories, South Road, Durham, DH1 3LE, United Kingdom

[3]School of Chemical Engineering and Advanced Materials, Newcastle University, Newcastle upon Tyne, NE1 7RU, United Kingdom

[4]Department of Earth Sciences, Durham University, Science Laboratories, South Road, Durham, DH1 3LE, United Kingdom

[5]Present address: Chemostrat Ltd., 2 Ravenscroft Court, Buttington Cross Enterprise Park, Welshpool, Powys, SY21 8SL, United Kingdom

*Corresponding Authors: elizamathia@chemostrat.com; a.c.aplin@durham.ac.uk

Abstract

Low and high resolution petrographic studies have been combined with mineralogical, TOC, RockEval and porosity data to investigate controls on the evolution of porosity in stratigraphically equivalent immature, oil-window and gas-window samples from the Lower Toarcian Posidonia Shale formation. A series of 26 samples from three boreholes (Wickensen Harderode and Haddessen) in the Hils syncline was investigated. The main primary components of the shales are microfossiferous calcite (30-50%), clay minerals (20-30%) and Type II organic matter (TOC = 7-15%, HI = 630-720 mg/gC in immature samples). Characteristic sub-centimetric light and dark lamination reflects rapid changes in the relative supply of these components. Total porosities decrease from 10-14% at Ro = 0.5% to 3-5% at Ro = 0.9% and then increase to 9-12% at Ro = 1.45%. These maturity-related porosity changes can be explained by (a) the primary composition of the shales, (b) carbonate diagenesis, (c) compaction and (d) the maturation, micro-migration, local trapping and gasification of heterogeneous organic phases. Calcite undergoes dissolution and reprecipitation reactions throughout the maturation sequence. Pores quantifiable in SEM (> ca. 50 nm) account for 14-25% of total porosity. At Ro = 0.5%, SEM-visible macropores[1] are associated mainly with biogenic calcite. At this maturity, clays and organic matter are not visibly porous but nevertheless hold most of the shale porosity. Porosity loss into the oil window reflects (a) compaction, (b) carbonate cementation and (c) perhaps the swelling of kerogen by retained oil. In addition, porosity is occluded by a range of bituminous phases, especially in microfossil macropores and microfractures. In the gas window, mineral-hosted porosity is still the primary form of macroporosity, most commonly observed at the organic-inorganic interface. Increasing porosity into the gas window also coincides with the formation of isolated, spongy and complex meso- and macropores within organic particles,

[1] Classification of pores by the International Union of Applied and Pure Chemistry (IUAPC): micropores (< 2 nm in diameter), mesopores (2-50 nm), macropores (> 50 nm).

related to thermal cracking and gas generation. This intraorganic porosity is highly heterogeneous: point-counted macroporosity of individual organic particles ranges from 0 - 40%, with 65% of organic particles containing no macropores. We suggest that this reflects the physicochemical heterogeneity of the organic phases plus the variable mechanical protection afforded by the mineral matrix to allow macroporosity to be retained. The development of organic macroporosity cannot alone account for the porosity increase observed from oil to gas window; major contributions also come from the increased volume of organic micro- and meso-porosity, and perhaps by kerogen shrinkage.

Keywords

Posidonia Shale, Porosity, Mineralogy, Petrography, Geochemistry

1. Introduction

The quality of a shale petroleum reservoir - its ability to store and then to yield oil and gas - is an integrated reflection of the way in which sedimentology, mineralogy, diagenesis and organic matter maturation combine to influence shale pore systems and mechanical properties. Whilst each one of these four subjects has been studied for decades in the context of palaeoenvironment, petroleum source rocks and basinal fluid flow (see e.g. Tissot and Welte 1984; Tyson 1995; Welte *et al*., 1997; Potter *et al*., 2005; Aplin and Macquaker, 2010), the focus on shales as reservoirs is more recent, requiring a more detailed approach and an integration of disciplines (e.g. Passey *et al*., 2010).

In recent years, conventional organic geochemical approaches to source rock characterisation (e.g. Jarvie *et al*., 2007) have been combined with high resolution electron microscope and synchrotron techniques (Bernard *et al*., 2010; 2011) to gain a deeper understanding of petroleum retention and the diversity of organic phases in shales. Improved electron microscope technologies have also generated substantial new insights into the nature of shale pore systems, especially when combined with other techniques such as low pressure gas sorption and small angle scattering (Loucks *et al*., 2009; 2012; Ross and Bustin, 2009; Desbois *et al*., 2009; Slatt and O'Brien, 2011; Heath *et al*., 2011; Bernard *et al*., 2012; Fishman *et al*., 2012; Klaver *et al*., 2012; Clarkson *et al*., 2013; Houben *et al*., 2013; Milliken *et al*., 2013; Rexer *et al*., 2014; Liang *et al*., 2014; Tang *et al*., 2014). Other studies have focussed on mineral diagenesis in organic-rich mudstones (Milliken *et al*., 2012; Macquaker *et al*., 2014; Pommer and Milliken, 2015).

Many previous studies have focussed on shales of a specific maturity and/or to demonstrate the use of a specific technique as a tool to evaluate shale properties. The aim of this paper is to combine mineralogical, microscopic, petrophysical and organic geochemical data to shed light on the controls of what are very substantial, maturity-related changes in the

porosity of marine, organic-rich, calcareous mudstones from the Posidonia shale (*ca*. 100 to 180°C; 0.53% to 1.45% Ro). The samples are particularly useful because previous studies have shown that the organic matter type and mineralogy of samples from the three wells are similar, albeit in the presence of sub-centimetric heterogeneities (e.g. Rullkötter *et al*., 1988; Littke *et al*., 1991; Vandenbroucke *et al*., 1993). We were thus able to track the evolution of the inorganic framework, organic matter and porosity as a result of increasing thermal stress, in addition to the role that small-scale heterogeneity plays in the development of porosity. Also, whilst the Posidonia Shale is not currently a major shale reservoir target, our results show that it shares common mineralogical, sedimentological and geochemical characteristics with the organic-rich facies of both the Haynesville (Hammes and Frébourg, 2012; Klaver *et al*., 2015) and Vaca Muerta (Kietzmann *et al.*, 2011) shales, both of which are important shale gas resource plays.

2. Samples and Methodologies

The Posidonia Shale of the Lower Saxony Basin, North Germany is a fine-grained, calcareous sediment deposited in an epicontinental sea during the Lower Toarcian, second-order sea level rise (e.g. Littke *et al*., 1991; Röhl and Schmid-Röhl, 2005). The Lower Toarcian transgression was a global event that induced worldwide shelf anoxia and produced excellent petroleum source rocks (Bachmann *et al.*, 2008). Temporal changes within the Posidonia Formation are suggested to reflect higher order sea level changes, coupled with subtle climatic fluctuations (Röhl *et al*., 2001). Based on macro- and microscopic observations, the formation is sub-divided into three units: lower marlstone (I), middle calcareous clay-shale (II) and upper calcareous clay-shale (III) (Figure 1b). While the marlstone differs from the overlying shales in having higher carbonate contents (55-61 wt.%),

units II and III are lithologically similar (35-38 wt.%) and are distinguished by the common occurrence of bivalves in the middle (II) shale (Littke *et al*., 1991, Rullkötter *et al*., 1988). All three units contain well-preserved, Type II marine organic matter with minor contributions of terrestrial macerals (Bour *et al.*, 2007; Littke *et al*., 1991; Röhl *et al.*, 2001).

For this study, samples were taken from the stratigraphically equivalent sections of three boreholes in the Hils syncline: Wickensen (0.53% R_o), Harderode (0.89% R_o) and Haddessen (1.45% R_o) (Figure 1a). The Hils half-graben forms part of a series of horst and graben structures that evolved during the Late Jurassic and Cretaceous (Bruns *et al*., 2014; Radke *et al*., 2001). Partly due to the complex tectonic and thermal history of the area, the origin of maturity variations in the Hils area is still debated. Some proposed that local variations in maturity relate to a Cretaceous intrusive body, the Vlotho Massif (Schaefer and Littke, 1988), whilst others suggest that the maturity gradient is a function of differential burial (Mackenzie *et al*., 1988; Munoz *et al*., 2007). Recent 3D modelling studies suggest that the region experienced a complex burial and thermal history, with differential heat flow associated with the Mesozoic rifting episodes (Bruns *et al*., 2014).

26 samples representing different stratigraphic units and maturities were selected for bulk analyses including Rock-Eval, TOC, grain density and total porosity (Figure 1b). The majority of samples were taken the lowest and highest maturity wells, mainly because of sample availability. Total Organic Carbon was measured with a LECO carbon analyzer equipped with a HF-100 Induction Furnace on a carbonate-free aliquot. Standard Rock-Eval was performed according to Espitalié *et al.* (1977) using a Delsi Rock Eval OSA. To correct for an oil-in-kerogen peak, 4 shale samples were solvent extracted with a mixture of dichloromethane (93%) and methanol (7%) and subsequently analysed for its remaining hydrocarbon potential.

The X-ray diffraction was performed by Macaulay Scientific Consulting Ltd. Bulk samples were wet ground (in ethanol) in a McCrone mill and spray dried to produce random powders with the optimum distribution of grains. X-ray powder diffraction (XRPD) patterns were recorded from 2-75°2θ using Cobalt Kα radiation. Quantitative analysis was done by a normalised, full pattern reference intensity ratio (RIR) method. Expanded uncertainty using a coverage factor of 2, i.e. 95% confidence, is given by $\pm X^{0.35}$, where X = concentration in wt.%, e.g. 30 wt.% ±3.3.

Grain density was measured on samples dried at 105°C using the "Small Pycnometer Method" with an error ± 0.02 g/cm^3. In this method (Rexer *et al*., 2013), 3 g of dry powdered shale sample was added to a pre-weighed pycnometer of a nominal value 50 mL, immersed in the 10 mL of surfactant (5% Teepol) and gently shaken. The slurry was outgassed in a dessicator overnight, filled with the outgassed deionized water up to the total volume of the pycnometer and weighed at temperature 25°C. The grain density was calculated from Equation 1:

$$\rho g = \frac{\rho w\,(m2-m1)}{(m4-m1)-(m3-m2)} \qquad (1)$$

where ρg (g/cm^3) is the shale grain density, ρw (g/cm^3) is the density of water at 25°C, m1 (g) is the pycnometer mass, m2 (g) is the mass of the pycnometer plus dry sample, m3 (g) is the mass of the pycnometer plus dry sample plus water, and m4 (g) is the mass of the pycnometer plus water.

Total shale porosity was determined from the measured grain density and bulk density when immersed in mercury at the pressure 25 psia using Equation 2:

$$\emptyset = 1 - \frac{\rho b}{\rho g} \qquad (2)$$

where ∅ (%) is the calculated total shale porosity, ρb (g/cm^3) is the measured bulk density at 25 psia, obtained using a Micromeritics Autopore IV Mercury Injection Porosimeter, and ρg (g/cm^3) is the predetermined grain density (Rexer *et al*., 2014).

For microscopic studies, 20 highly-polished thin sections and 3 resin covered blocks, cut perpendicular to bedding, were prepared. Thin sections were first scanned using an Epson Perfection V500 scanner with 9600 dpi resolution. Subsequently, each thin section was examined with a Nikon Eclipse LV100 POL transmitted light petrographic microscope with an attached Nikon Digital Sight DS-U3 camera. Polished blocks were examined in reflected and UV light using an Oil Zeiss Immersol 518N oil immersion microscope. The fluorescence of organic matter was determined qualitatively using UV light with an HXP 120C accessory.

Carbon-coated polished thin sections were examined using a Hitachi SU-70 High Resolution Analytical SEM, equipped with an Oxford Instrument Energy Dispersive X-ray microanalysis system (INCA Energy 700). Samples were viewed in Back Scattered Electron (BSE) mode using the YAG detector with the following conditions: 15-8 mm WD, 15keV accelerating voltage, 2-4 nA filament current. To reduce the shale topography, prior to the SEM imaging, selected samples were polished with an argon broad ion beam (BIB) in a GATAN 691 Precision Ion Polishing System (PIPS^{TM}). In order to fit into the system's chamber, the sample size was reduced to a 3 mm diameter disc with a GATAN 601 Ultrasound Disc Cutter using a water emulsion of boron nitrate powder as a saw. Discs were inserted into the PIPS^{TM} chamber and bombarded with Ar ions in a vacuum (10^{-2} Pa) for 6 hours (angle 3°, 5kV, 1-20 µA). Images used to quantify porosity were captured in Secondary Electron (SE) mode using a through-the-lens detector (TLD) at magnification 6,000x (pixel size 15 nm). The total image porosity (practically, macroporosity due to the magnification used) was quantified on image mosaics covering a total area 6000 µm^2 with the point

counting method (10,000 counts) in the image analysis software JMicroVision 1.2.7. (Roduit, 2008).

For selected areas, element maps were generated using Energy Dispersive X-rays (EDX). Settings for the EDX collection were 300 µm dwell time for 35 frame acquisition, 15kV accelerating voltage and 2.5 nA filament current.

For high resolution imaging, three samples were milled, polished and imaged with a gallium (Ga) focused ion beam (FIB) in the FEI Helios Nanolab 600, using a FEG source. 15 µm x 5 µm trenches were cut using 8-16kV accelerating ion beam voltage and 0.93-5.5 nA beam current. Samples were viewed in BSE Immersion or secondary electron mode with the following conditions: 4.1 mm WD, 1.5-3.0 kV accelerating voltage, 0.17-1.4 nA beam current, using a through-the-lens detector for better spatial resolution. The images were captured at magnifications between 10,000-200,000x, corresponding to pixel sizes 25-1.2 nm. These images were not used for quantitative porosity estimates due to the limited and thus non-representative areas covered by the image.

3. Results

3.1 Composition and Texture

Low maturity Posidonia shale from the Wickensen (WIC) borehole (Ro = 0.53%) is a medium grey, calcareous nannoplankton-bearing to calcareous nannoplankton-rich mudstone (with the majority of mineral grains < 62.5 µm in diameter), showing mineralogical differences on scales ranging from millimetres to metres (Figures 1, 2). Bulk mineralogy (Table 1) indicates similar proportions (30-40 wt.%) of both calcite and clays in the upper shale units, with higher amounts of calcite compared to clays in the lower marlstone unit

(~50% and ~25% respectively). As the main minerals, calcite and phyllosilicate abundances are inversely correlated. The visible calcareous fraction is much coarser in the lowest marlstone unit (up to 0.6 mm; Figures 2, 3f) in comparison to both clay-rich units (typically <0.1-0.3 mm; Figures 3a, 3b, 3c). Macrofossils were rarely observed in this study except for rare occurrences of foraminifera (Figures 4e, 7a), bivalves (Figure 4c), fish-bone fragments and other, unrecognized calcareous skeletal fragments.

Although the finest particles and cements constituting the shale matrix cannot be resolved with standard petrographic methods, the microcrystalline nature of the microscopically distinguishable carbonate aggregates suggest that they are compacted faecal pellets (Bour *et al.*, 2007; Littke *et al.*, 1987; Röhl *et al.*, 2001; Röhl and Schmid-Röhl, 2005; Schieber, 1999). Their distribution varies from (a) sparse and in some cases aligned into discontinuous layers in the calcareous shales, to (b) densely packed in the marlstone unit.

All three units of the Posidonia contain more-or-less apparent, sub-centimetric light and dark laminae, reflecting differences in the proportion of carbonate and clay components (Figure 2). This lamination is most pronounced in the upper shale unit (Figures 3a, 3b), with individual laminae typically up to 3 mm thick (Figure 2a). In both the lower calcareous shale (Figure 3c) and marlstone horizons (Figures 3d, 3e, 3f) the sub-centimetric lamination is typically less pronounced. In the marlstone unit, horizontal lamination is partly imparted by variations in the abundance of faecal pellets (Figures 2b, 3d, 3e, 3f). Here, due to the large size of individual pellets (often exceeding 0.5 mm), lenticular lamination is common (Figures 2b, 3e, 3f) and convoluted lamination also occurs. In all units, contacts between laminae are parallel and vary from sharp to gradual (Figures 2a, 2b, 3b). The regular character of the lamination suggests that it is primary, reflecting changes in the relative supply of the clastic and biogenic components. Rarely, boundaries between laminae are marked by an erosional contact or the presence of a thin layer of silt-grade carbonate or quartz (Figure 3c).

Modest changes in composition and fabric occur at maturities of Ro > 0.9% and 1.45%. While the total clay and carbonate contents do not differ from those encountered in the immature section, there is a relative increase in the proportion of dolomite to calcite, irrespective of the unit (Table 1). Although there is no conclusive petrographic evidence for the timing of dolomite formation, its absence in low maturity shale, plus the higher content of Na-rich plagioclase in rocks of higher maturity (Table 1), suggests that both minerals formed at oil window maturities. The textural effect of these processes can be seen at the thin section scale. In both Harderode and Haddessen, the primary sub-centimetre lamination is either still preserved (Figures 4b, 5d), modified (Figures 2c, 4a) or obliterated (Figure 2d) due to diagenetic changes affecting the matrix calcite and generation/expulsion/redistribution of organic matter (Figures 4, 5). Authigenic carbonate is common, with crystals reaching > 100 µm, and up to 0.05-0.1 mm (Figures 4d, 5b, 5c, 5e), commonly cementing algal bodies (Figure 4c), fossil cavities (Figure 4e) or fractures (Figure 4f). Some layers are more affected by diagenetic changes (Figure 4a) and may reflect differences in the original composition, e.g. higher calcite or quartz contents. Consistent with the observations from the low maturity borehole, faecal pellets are more abundant in the marlstone unit (Figure 5f) than in the calcareous clay-shale (Figures 5a, 5e).

3.2 Microstructure

High-resolution BSEM micrographs show that most of the carbonate fraction in the early mature Wickensen samples is of biogenic origin, deposited as faecal pellets (Figures 6a, 6c). Nannofossils, mostly coccoliths and schizospheres, form debris dispersed in the shale matrix or concentrated in microlayers or ellipsoidal aggregates (Figure 6c). Although individual particles are often mechanically broken (Figure 6b), some samples still contain a high

proportion of less disarticulated material. The size of nannofossil aggregates varies from <5 µm (Figure 6b) in the calcareous shale units to over 500 µm in the marlstone samples. In all units, microlamination is typical, but its pattern is different in the sub-centimetre light and dark laminae. In lighter laminae, nannofossil material tends to form continuous, <50 µm thick layers (Figure 6a), whilst in the dark laminae, isolated islands of faecal pellets are commonly surrounded by the clay-rich matrix (Figure 6b). The biogenic fraction shows signs of diagenetic alterations, but its intensity is different in the marlstone and calcareous shale units. Calcite diagenesis is more prominent in the marlstone unit (Figure 6c) and involves precipitation of calcite cement in the intrafossil and intergranular porosity of coccoliths and schizosphere debris. Cement precipitation, and possibly local dissolution and reprecipitation of fossiliferous grains, is documented by the appearance of faceted calcite crystals coexisting with still unaffected fossil structures. In the two more clay-rich Posidonia units, carbonate cement is also present, but the intensity of calcite diagenesis is lower. Nevertheless, we observed subtle authigenic overgrowths on biogenic fragments (Figure 6b), authigenic cement within biogenic aggregates, and the presence of small microcarbs of unknown origin, infilling porosity. Overall, authigenic calcite precipitation is more prevalent in the sub-centimetre, light laminae, which contain greater concentrations of nannofossil material, and is weaker in the clay-rich zones where biogenic fragments are more dispersed.

Loss of nannofossil structures and precipitation of new authigenic phases is more advanced in samples of maturity 0.9% Ro (HAR) and 1.45% Ro (HAD). In both HAR and HAD, the infilling of coccolith canals and foraminifera cavities with calcite cement is ubiquitous (Figures 7a, 7b). The biogenic structures, although still present, are less discernible, and fusing features within faecal pellets are common (Figure 7e). The loss of individual nannofossil structures suggests calcite dissolution and reprecipitation, but little specific textural evidence is observed, apart from the presence of faceted calcite crystals in

place of coccoliths (Figure 7d). Individual subhedral and euhedral crystals of authigenic calcite vary in size from < 1 µm up to tens of microns (Figure 7e). In some cases, calcite cement fills algal cysts (Figure 6e), preventing them from compacting mechanically. Some zones are fully cemented, and their size can reach up to 1000 µm in length (Figure 7f). Alternatively, these large calcite masses may represent modified and unrecognizable, large fossil fragments. Authigenic dolomite is common, and can be observed either as small (< 20 µm), discrete crystals (Figure 7b), or as large, cemented zones up to 100 microns in length.

The composition of the clay fraction is similar at all maturities. Detrital clays are potassium-rich; authigenic kaolinite is present and is usually observed filling algal cysts and cavities in fossil canals, or alternatively as framework replacive/displacive cement (Figure 7f). The detrital silt fraction is dominated by quartz, forming anhedral, rounded to subangular grains varying in size from under 1 µm up to 20 µm (Figures 6a, 7a). In samples at higher maturities, authigenic quartz often cements detrital quartz grains (Figure 7a). In some cases, recrystallized quartz forms part of diagenetically modified microlayers (Figure 6f). Finally, authigenic pyrite is present at all maturities, forming small euhedra (Figures 6f, 7c), oval framboids (Figures 6c, 7b, 7d), nodules, or directly replacing biogenic calcite and quartz (Figure 7c).

Physical compaction can be seen as horizontal flattening of algal cysts, clay aggregates, and faecal pellets (Figures 3a, 6d, 8). The collapse of the shale structure can also be seen adjacent to rigid shale components associated with compaction shadows. The shortening of the matrix in the vertical direction is clear at maturities between 0-5-0.9% Ro, often related to the collapse of algal cysts (Figure 6d).

3.3 Organic matter

In the least mature shale at 0.53% R_o (WIC), TOC varies between ~ 7-15 wt.% (mean 10 wt.%), decreasing to an average of ~ 7% in the peak oil window (HAR 0.89% R_o) and down to ~ 6% in the gas window (HAD 1.45% R_o; Table 2). RockEval data confirm the maturation pathway typical for the Type II marine kerogen. We also observed a consistent drop in both S1 and S2 yields, resulting in a decrease in HI from ~650 to ~60 mg/gTOC. A significant drop in yield, from 10 to 1 mg/g, was observed for the amount of organic matter pyrolizable under standard RockEval conditions, but on samples pre-extracted with organic solvents ($S2_a$). For all samples, $S2_a$, which is that part of the S2 peak which can be solvent-extracted and can thus be considered as a form of bitumen, is consistently higher than RockEval-measured S1 (Table 3). Oil saturation indices, calculated as the ratio of (S1 + $S2_a$) to TOC, vary from 105 mg/gTOC for the early oil window sample, 66 and 102 for the two peak oil window samples and 27 mg/gTOC for the gas window sample.

Most of the organic matter is unresolved in the standard petrographic sections. Resolved organic matter occurs as flat, up to 0.3 mm long, organo-clay aggregates (Figures 3d, 3f) and as highly compacted, discrete cysts (Figure 3a). Large terrestrial organic particles (up to 500 µm) are scarce, but relatively more common in the marlstone unit (Figures 2b, 3e, 3f).

Organic macerals show a gradual change in type, volume and colour as a function of maturity. At Ro = 0.53%, structured algal liptinite (e.g. Tasmanales, Leiosphaeridales) is common, forming well-preserved laminae or thick bodies (Figures 9a, b), and co-existing with less pronounced lamellar bituminite. The shale matrix is strongly fluorescing, comprising a bituminous-mineral groundmass, with its organic component, the so-called matrix bituminite, representing a non-structured degradation product of marine phytoplankton and zooplankton (Tao *et al.*, 2012); this forms the most abundant organic component in the shale. In low maturity Posidonia, the bituminous groundmass is primarily associated with clays (Figure 6a), but may also fill the interstices within fossils. Terrestrial macerals,

including vitrinite and inertinite, are dispersed and are present in low abundance. Both structured liptinite and terrestrial macerals contain sulphur, typically incorporated into organic matter as a by-product of bacterial sulfate reduction processes taking place in anoxic sediment (Macquaker *et al.*, 2014, and references therein).

At the peak oil window maturity, structured algal liptinite is volumetrically less abundant and has a weak, brownish fluorescence (Figure 9c). The bodies of Tasmanales are collapsed (Figure 6d), or locally filled with diagenetic carbonates (Figure 6e). The bituminous groundmass is much less fluorescent and instead, a dense network of non-solvent extractable, solid bitumen fills intergranular space (Figures 9d, 10a). The increased concentration of solid bitumen within faecal pellets provides a strong contrast to the typical organo-clay associations observed at lower maturity. Solid bitumen can also be found within microfractures, often in association with diagenetic carbonates (Figure 9d).

At the gas window maturity, the bituminous groundmass exhibits a very weak fluorescence, and no structured algal liptinite is present (Figure 9e). A tight network of irregularly-shaped, non-extractable, solid bitumen is a dominant feature (Figures 9f, 10b). The bitumen phase pervasively fills the tight, clay-carbonate matrix and microfractures.

3.4 Porosity

3.4.1 Total Porosity

Average grain densities increase as a function of maturity from ~2.3 g/cm^3 at 0.53% R_o, to ~2.5 at 0.89% R_o and ~2.6 at 1.45% R_o, reflecting the reduction in organic matter volume and the increase in kerogen density (Okiongbo *et al*., 2005; Rexer *et al*., 2014; Table 2). At 0.53% R_o, porosities vary between 10-14% and, despite the decrease in TOC and expulsion of petroleum, decline to 2.5-4.5% in the peak oil window (0.89% R_o) (Table 2). In contrast, at gas window maturities, with further reduction of the organic carbon content, total porosity

increases to 9-14%, similar to those at 0.53% R_o. Porosity does not correlate with mineralogy or TOC at any maturity, although any potential patterns would be difficult to discern given the relatively narrow range of both mineralogy and TOC content.

Grain densities and total porosities change when soluble bitumen is extracted (Table 3). The most significant increase in grain density was measured in the peak oil window sample, with an insignificant increase in the gas window shale and a very slight decrease in the early mature shale (Table 3). On the basis of the change in the grain density of bulk shale "pre-" and "post-extraction", we estimated the amount of the extractable bitumen and thus the "minus-soluble bitumen" total porosity for three samples of medium (HAR 7060, 7070) and high maturity (HAD 7110). We assumed that the extractable bitumen occludes porosity, and therefore its amount is equivalent to the fraction of porosity filled with soluble bitumen. The results show that the amount of the extractable bitumen present in samples decreases from 2.8 volume % in the marlstone and 3.4 volume % in the calcareous shale at the peak oil window maturity to 0.68% (calcareous shale) in the gas window (Table 3); this corresponds to oil saturations (i.e. % of porosity filled with soluble bitumen) of *ca*. 44%, 44% and 7% correspondingly. Some of this bitumen is likely to be physically associated with kerogen and so the oil saturations should be taken as maxima. Hypothetical, bitumen-free total porosities after solvent extraction are higher than those measured in the as-received shale (Table 2), amounting to 6.3-7.8% and 10.1% in the peak oil window and gas window samples respectively (Table 3).

3.4.2 SEM Observation of Meso- and Macroporosity

Porosity point-counted from BIB-SEM images is not significantly different in samples of different maturity, amounting to 1.3% in the Wickensen sample, and 1.1% and 1.5% in the Harderode and Haddessen samples respectively (Figure 11a). Due to the limited image

resolution (pixel size 15 nm), almost all point-counted pores lie within the macropore size range (> 50 nm). Mesoporosity (2-50 nm) is thus greatly underestimated or, along with the microporosity (< 2 nm), unresolved. Consequently, the point-counted image porosity is only 14-25% of the experimentally measured total porosity, with the highest fraction of resolved porosity found in the oil window shale (Figure 11b).

Pores were classified into interparticle, intraparticle and organic matter-hosted using the general classification of Loucks *et al*. (2009). Our division is based on the spatial relation of pores with respect to mineral phases and organic matter, and not on the origin of pores. The following definitions of different pore types were adopted here:

- Interparticle: 1) pores between detrital grains, authigenic minerals, nannofossils and clay flakes; 2) pores (in 2 or 3D space) associated with the interface of organic matter and mineral matrix that do not visibly extend into an organic particle, and that are either irregularly shaped or mirror the shape of the adjacent mineral phase;
- Intraparticle: 1) pores within single mineral grains or fossil bodies; 2) pores within well-defined faecal pellets and pyrite framboids; 3) moldic pores formed due to dissolution of mineral phases; 4) pores at the interface of inorganic matrix and organic macerals that do not visibly extend into an organic particle, contained within a fossil body, faecal pellet or pyrite framboid;
- Organic matter-hosted: 1) discrete, round, bubble-like pores in the organic matter; 2) sponge-like pores within the organic matter, often interconnected and grouped; 3) pores typically at the interface of organic matter and mineral matrix, irregular in shape, but visibly extending in 3D into the organic particle; 4) visible cracks within OM particles, often with jagged edges and extending into the particle.

Pore types estimated by point-counting change through the maturity sequence from exclusively inter- and intraparticle in the low maturity sample, to inter- and intraparticle-dominated in the peak oil window and finally, to inter- and intraparticle-rich with a moderate proportion of organic matter-hosted pores in the sample from the gas window maturity (Figure 12). Visual observations of different pore types using high-resolution SEM micrographs show a varied assemblage of pores with sizes as small as 5 nanometers (200,000x magnification), up to a few µm.

In the least mature sample (Figure 13), visible pores are associated mainly with biogenic calcite, with no significant porosity within the clay matrix. The typical intraparticle pores associated with calcite are found within fully-open coccolith canals, coccolith canals partly cemented with authigenic calcite, within fragments of Schizosphaerella, as well as between fragmented or crushed nanofossils and authigenic calcite phases within well-defined faecal pellets (Figures 13a-e). Intraparticle pores are also found within zones cemented with authigenic calcite, between cement crystals, and within discrete calcite crystals as a result of carbonate dissolution (Figure 13h). In some cases, those pores are lined with organics, imparting a smooth, pendular shape to pore edges (Figure 13e).

In contrast to the intraparticle pores, interparticle, carbonate-associated pores are found mostly between carbonate phases and the organo-clay matrix (Figures 13i, j). The size and shape of inter- and intraparticle pores is strongly related to the extent of precipitation of diagenetic carbonates (Figure 13i). The size of visible, calcite-associated pores ranges from tens of nanometres to ~ 3 µm. Pores found in the fossil bodies of Schizopheralles are usually equant and straight edged, up to 500 nm in diameter. Large inter- and intraparticle pores associated with altered nanofossils and carbonate cements can be straight edged or spheroidal, reaching up to 3 µm.

Non-calcite-associated porosity is relatively minor but small amounts of interparticle pores occur between detrital clays, or adjacent to quartz, or pyrite, often at the interface with organic matter. These pores can reach 2-5 µm in diameter but also may form narrow, < 100 nm rims around or adjacent to mineral phases or organic matter (Figure 13k). Elongated intraparticle pores occur within clay group minerals, more pronounced where pyrite has precipitated between clay platelets (Figure 13f). Large intraparticle pores, often lined with organic matter, can also be sporadically found within pyrite framboids (Figure 13g).

At the maturity of 0.5% Ro, the majority of organic matter is not internally macroporous. Occurrences of intraparticle organic matter-hosted pores are very rare but include remnant porosity within walls of semi-compacted Tasmanales bodies (Figure 13l) and well-defined, round or angular, < 1 µm pores found within arcuate, likely terrestrial organic particles.

In the shale at oil window maturity, most of the pore types observed at lower maturities are absent, lost due to compaction (mechanical and chemical) or occluded by solid bitumen (Figure 10a). Several new types of intra- and interparticle pores occur (Figure 14). Commonly, pores are associated with organic matter and/or authigenic phases. Elongated pores with jagged edges cross-cut organic particles and resemble microfractures (Figures 14a, b). Many pores are found at organo-mineral interfaces and exhibit complex shapes which match those of the surrounding mineral phases (Figure 14e). Most of these interface pores are associated with diagenetic calcite and are occasionally filled with authigenic phases (Figure 14f). In 3D, pores found directly within organics can always be traced to particle edges (Figures 14c, d).

Pores in oil window shales are also hosted within inorganic domains (Figure 14g). Fracture or cleavage-related porosity is associated with clay-mineral platelets (Figure 14h), sometimes partially filled with authigenic phases such as pyrite (Figure 14i). Crack-like pores are also observed at clay-carbonate interfaces. In 3D Slice and View reconstructions, crack-

451 shaped pores often follow the shape of underlying organic phases. Within carbonate minerals,
452 intraparticle dissolution pores can be found (Figure 14k), ranging in size from < 100 nm up to
453 2 µm. Rare intraparticle porosity, not clogged by bitumen, is also encountered within
454 domains of authigenic calcite (Figure 14l) and pyrite framboids (Figure 14j).

455 Gas window shale, in contrast to samples of lower maturities, contains porosity *within*
456 organic particles (Figure 15). This porosity is highly heterogeneous, such that the point-
457 counted porosity of individual organic particles ranges from 0-40%; 65% of organic particles
458 contain no SEM-visible porosity, i.e. no pores larger than around 50 nm.

459 Although the shape and size of organic matter-hosted pores form a continuum, we
460 distinguished several end-members:

461

462 1. Isolated, bubble-like pores, generally < 100 nm in diameter. Their spatial
463 distribution within organic components is varied, sometimes uniformly
464 distributed within an organic 'particle' (Figure 15a), or occupying only a fraction
465 of a 'particle' (Figure 15c), or concentrated at 'particle' margins (Figure 15f).
466 2. Similar to 'bubble' pores, but usually clustered in groups, are sponge-like pores
467 (Figure 15b). They are very often visibly interconnected in 2D and in 3D Slice
468 and View images, with elongated shapes of sizes exceeding 100 nm. The
469 direction of elongation is often along the margin of two adjacent phases, for
470 example at the interface of porous and non-porous organic phases, or near an
471 organic-inorganic interface. Similarly to discrete pores, sponge-like pores may be
472 evenly distributed or occupy only a fraction of an organic 'particle'.
473 3. With the increase in size and connectivity of individual pores, sponge-like pores
474 may be replaced by irregularly shaped or spheroidal organic matter-hosted pores.
475 Although often present directly within organic matter (Figure 15d), in 3D they

476 are usually associated with organic-inorganic interfaces (Figures 15e, 15h). In 3D
477 Slice and View images, the interiors of complex pores branch out into numerous
478 spongy-pores, penetrating the organic mass (Figure 15e). Depending on the size
479 of a host organic 'particle', the diameter of a single complex pore may reach 500
480 nm.
481 4. Similar in shape to sponge-like pores, but usually associated with 'particle'
482 margins and less likely to agglomerate into complex pores, are oval, 'pendular'
483 pores (Figure 15c). Ranging in diameter from a few tens to a few hundreds of
484 nanometers, a single 'pendular' pore can occupy a large fraction of a 'particle' or
485 alternatively, may be located only at the 'particle' interface. Within a single
486 organic 'particle', 'pendular' pores can co-exist with other organic matter-hosted
487 pore types.
488 5. The last type of intraparticle organic matter-hosted pore is found within terrestrial
489 macerals (Figure 15g). The shape of these pores varies from angular to oval, and
490 their size may reach up to 1 µm in diameter.
491
492 Although intraorganic pores are a very characteristic feature of the gas window
493 Posidonia shale, mineral-associated porosity is still the primary form of SEM-visible porosity
494 (Figure 12). As for the irregular and complex organic matter-hosted pores, mineral-associated
495 pores are commonly present at the organic-inorganic interface, but do not visibly penetrate
496 adjacent organic matter (Figures 15h, 16a, 16d-f). These interface pores have jagged edges,
497 with an irregularly-shaped organic face (Figure 15h), or smooth outlines (Figure 16b, c),
498 resembling the smooth interface pores already present in the oil window (Figure 14e).
499 Depending on their relation to the surrounding inorganic phases, the mineral-associated pores
500 can be classified either as intraparticle or interparticle. The locations of the highest density of

the interface pores include faecal pellet domains and pyrite framboids (Figures 15i, 16e), but the jagged-shaped pores can also be found in the vicinity of detrital grains and clay packages (Figure 16f). The interface pores are the largest pores present in the gas window Posidonia, and their size can exceed 2 µm in diameter.

Other types of mineral-hosted pores in the gas mature sample are relatively uncommon but include: intraparticle pores within mica group minerals (Figure 16g), intracrystal carbonate dissolution pores with characteristic rhomboidal outlines (Figure 16h) and possibly blind pores between carbonate cement crystals (Figure 16i).

4. Discussion

4.1 Mineralogy and Texture

The laminated texture of the immature Posidonia shale, observed mainly at the sub-centimetre scale in this study, primarily reflects variations in the relative rates of supply of biogenic calcite and detrital, clay-rich material. The predominantly concordant contacts between laminae confirm the primary nature of the lamination and the lack of bioturbation supports the probability that bottom waters were depleted in oxygen, as required for the preservation of significant organic matter. In contrast to Trabucho-Alexandre *et al.* (2012) who investigated Posidonia Shale from the Dutch Central Graben characterized by a higher clastic input, we did not encounter evidence of wave or current activity, apart from rare layers of silt-sized material of unknown origin and very rare scours (Figure 4a).

Littke *et al.* (1991) ascribed variations in the amount of carbonate and clay minerals to relative changes in the rate of nutrient-dependent primary production in surface waters as compared to the supply of terrigenous clays. Similar vertical laminations have also been observed in the Posidonia Shale deposited in the Southwest German Basin (Röhl *et al.*,

525 2001). In this study, the importance of variations in carbonate and clay is less its
526 palaeoenvironmental significance but rather the way it influences diagenesis, the migration
527 and trapping of petroleum and the related way in which the pore system evolved. This is
528 explored in the next section.
529
530 **4.2 Porosity and MacroPores**
531 A key observation of this study is the way in which porosity changes as a function of
532 maturity. Porosities of as-received samples, at the start of oil generation (R_o = 0.5%, *ca*.
533 100°C), are 10-14%, declining to 3-5% at R_o = 0.9% (*ca*. 150°C) and then increasing to 9-
534 12% at R_o = 1.45% (*ca*. 180°C). In rationalizing these results, we must recall that the
535 petrographic data we present in this paper, whilst quantitative in terms of point-counted
536 porosity, only accounts for around 15-25% of total porosity. Since the effective resolution in
537 this study is around 50 nm, we can only quantify macroporosity, which in these samples is
538 mainly associated with carbonate-rich areas of the sediment and, in the gas window samples,
539 organic matter. As discussed by Rexer *et al*. (2014) in a study of WIC 7145, WIC 7155, HAR
540 7038, HAR 7060, HAD 7090 and HAD 7119, which are also part of this study, the majority
541 of porosity in these shales is micro- and mesoporous, associated mainly with clay minerals
542 and organic matter, and cannot be considered here. Nevertheless, the division of resolved and
543 unresolved porosity and their occurrence in specific mineral and organic domains points to
544 the importance of original rock fabric as a starting point to model porosity retention, loss and
545 development.
546 We argue here that maturity-related porosity changes reflect the complex interplay of (a)
547 the primary clay/carbonate fabric, (b) carbonate diagenesis, (c) organic matter maturation,
548 migration and trapping, (d) gas generation and (e) chemically-enhanced mechanical

549 compaction. Some of these processes occur simultaneously and cause positive or negative
550 feedback to others.
551
552 ***4.2.1 Carbonate Diagenesis***
553 Resulting from redox reactions during shallow burial, early diagenetic carbonate is
554 common in many organic-rich mudstones (e.g. Hesse, 1990; Macquaker *et al*., 2007;
555 Macquaker *et al*., 2014) and is observed here as uncompacted, calcite-filled coccolith canals.
556 Nevertheless, early diagenetic pore-filling carbonate is relatively rare so that much of the
557 SEM-visible porosity in the lowest maturity samples is associated with fragments of biogenic
558 carbonate, often concentrated within faecal pellets (Figures 3, 6, 13).
559 Whilst there is some evidence for authigenic calcite in the low maturity samples (Figures
560 6b, 6c), it is not pervasive. Disappearance of nannofossils, recrystallization of carbonate and
561 precipitation of cement continues from the lowest to highest maturity samples, i.e. at
562 temperatures between 100 and 180°C, concomitant with oil and gas generation. The
563 diagenesis of calcite in organic- and clay-rich shales has not been studied in detail, but our
564 observations suggest that it may proceed at a different rate to that observed in purer fine-
565 grained carbonate rocks such as chalk. Pressure solution in chalk starts at temperatures as low
566 as 20°C, with dissolution seams and stylolites common at 30-40°C (e.g. Mallon and
567 Swarbrick, 2002). Carbonate recrystallization in chalk is very advanced by 100-120°C,
568 similar to the temperature experienced by our lowest maturity sample. In contrast, calcite
569 cementation and recrystallization in the Posidonia are limited at Ro = 0.53%, becoming
570 increasingly evident at 0.9% and 1.45%. Whilst we do not have sufficient information to be
571 conclusive about the apparently retarded carbonate diagenesis in the Posidonia compared to
572 chalk, experimental data suggest that argillaceous chalks, due to the inhibition of carbonate
573 precipitation, are less prone to chemical compaction than pure chalk (Baker *et al*., 1980). This

574 is consistent with our observations that calcite diagenesis is more advanced in the more
575 carbonate-rich Posidonia marlstone compared with the more clay-rich middle and upper
576 Posidonia units. It has also been observed that diagenesis and cementation can be retarded in
577 oil-filled carbonate and quartzose reservoirs as a result of alterations in the wetting state of
578 the reservoir from water-wet to oil-wet, and a concomitant reduction of the amount of water
579 available for solution transfer (e.g. Scholle, 1977; Worden *et al*., 1998; Heasley *et al.*, 2000).
580 It is certainly plausible that in an organic-rich shale like the Posidonia, carbonate surfaces
581 become oil-wet even prior to oil generation, as a result of sorption of polar organic molecules
582 (van Duin and Larter, 2001; Aplin and Larter, 2005). Nevertheless, it is also plausible that,
583 similar to oil-saturated chalks, minor recrystallization of calcite continued even under oil-wet
584 conditions (Fabricius, 2003).

585 Petrographic data are inconclusive about the diagenetic processes which result in the
586 precipitation of carbonate cements and loss of nannofossil structures. Recrystallization
587 features, such as euhedral calcite in place of biogenic structures, and contact-cement
588 structures occur in the lowest maturity samples and are significantly better developed in the
589 more calcite-rich laminae. Recrystallization and redistribution (for example calcite in
590 bitumen-bearing microfractures) has clearly occurred, but the relevance of pressure solution
591 to that process cannot be quantified. We also note that diagenetic dolomite occurs in samples
592 at 150 and 180°C, which requires a source of magnesium. Whilst the Mg could in principle
593 be released as a result of the smectite to illite transformation reaction (McHargue and Price,
594 2006), dolomite in these samples formed at temperatures higher than the main illitisation
595 window; an alternative source of magnesium has been suggested to be high salinity brines
596 (Munoz *et al.*, 2007; Bernard *et al*., 2013).

597 The implications of carbonate diagenesis for porosity evolution are difficult to quantify.
598 Whilst pore-filling calcite is observed, the loss of biogenic structures suggests that most

599 diagenetic calcite is recrystallized from a biogenic precursor, implying a change from a less
600 to a more stable calcite type (Fabricius, 2003). Recrystallization of calcite without porosity
601 modification has been described in chalk (Fabricius *et al.*, 2008) and may inhibit compaction
602 by forming a stiffer framework due to the development of contact cements. Finally, whilst
603 stylolitisation is a well-known porosity reduction mechanism in carbonates, resulting in
604 calcite cement precipitation in pores away from the stress point (Fabricius *et al.*, 2008;
605 Scholle and Halley, 1985), it is not commonly observed in our samples, at least on a
606 microscopic scale.
607
608 ***4.2.2 Organic matter maturation, migration and trapping***
609 Whilst the way in which different kerogen types decompose to bitumen, oil and gas has
610 been extensively studied, both generally and specifically within the Posidonia (e.g. Behar *et*
611 *al.*, 2008a; 2008b; 2010; Bernard *et al.*, 2011; Dieckmann *et al.*, 1988; Horsfield *et al.*, 1992;
612 Leythaeuser *et al.*, 1988; Lewan, 1997; Rullkötter *et al.*, 1988), the mechanisms of primary
613 migration, phase behaviour, bitumen entrapment and evolution of organic matter-hosted
614 porosity are still debated. Behar *et al.* (2008b) proposed a kinetic scheme where kerogen
615 initially decomposes into a very viscous, NSO-rich liquid which is further decomposed into
616 more soluble non-hydrocarbon compounds and finally, cracked into hydrocarbons. The
617 occurrence of a heavy, intermediate bitumen phase was also proposed by Michelis *et al.*
618 (1996) and Lewan (1997). In this study, RockEval data for unextracted and extracted samples
619 confirm the presence of a substantial amount of a non-volatile bitumen phase within the low
620 maturity Posidonia shale (*cf.* Clementz, 1978; Wilhelms *et al.*, 1990). This early-formed
621 bitumen has a similar density to kerogen (Figure 12) and, based on the lack of petrographic
622 evidence for porosity-filling bitumen at this maturity, we suggest that it has limited mobility
623 and is, in the main, physically associated with the precursor kerogen.

Continued cracking of the viscous phase into the heart of the oil window results not only in a less viscous petroleum (Dieckmann *et al*., 1988; Rullkötter *et al.*, 1988; Schenk *et al*., 1997) but also a poorly soluble, high molecular weight residue, often described as solid bitumen, residual petroleum or prechar. Whilst terms such as “petroleum” and “prechar” simplify what is a complex chemical process which may involve more than two end-member phases, we can imagine that different phases generated at different temperatures will have radically different viscosities and mobility. Whilst much of the generated petroleum is of course expelled from the shale, some remains physically associated with microporous kerogen (Sandvik *et al*., 1992; Jarvie *et al*., 2007); another part, of particular interest here, is trapped within the pore and microfracture system of the shale (Figures 9; 10). In our study, micromigration and local trapping is corroborated by microscopic observations which show the highly dispersed nature of the solid bitumen, forming a semi-continuous network (Landis and Castaño, 1995; Loucks and Reed, 2014; Milliken *et al.*, 2014). The dispersed nature of the retained bitumen phase partly reflects that of precursor amorphous organic matter filling spaces between mineral grains in the immature shale (Figures 6b, 9a). However, in contrast to the immature kerogen, which is mainly associated with the clays (see also Littke *et al*., 1991), it is very common in the peak oil window and gas window to see organic matter infilling porosity within microfossiliferous domains, indicating micromigration and trapping. It is plausible that bitumen within the source rock followed the path of least capillary resistance, entering large pores within microfossils which then acted as micro-capillary traps. At gas window maturities, the observation of solid bitumen associated with what are now areas of cement and recrystallized calcite suggests that migration of the bitumen phase was inhibited once it became trapped in porous, rigid, microfossiliferous zones. Similar solid bitumen, although of different genesis, is well known in oil and gas reservoirs (Hwang *et al.*, 1998;

Lomando, 1992) and also as a product of solidification of heavy oil in coals (Mastalerz and Glikson, 2000).

On average, approximately 3 weight % TOC is lost from our samples between Ro = 0.53% and Ro = 0.89% (Table 2). Converting this to a volume % organic matter by assuming a density for organic matter approximately half that of the mineral matrix (Okiongbo *et al*., 2005), this would lead to an *increase* in porosity of around 7.5%, assuming a completely rigid mineral framework and thus zero compaction. There is petrographic evidence for minor porosity generation. For instance, the appearance of pores at the interface of organic and inorganic phases (Figures 14d-f) suggests a volume loss of organic matter due to petroleum generation, although similar observations in the Marcellus shale have also been interpreted as desiccation, depressurization or post-coring, phase alteration features (Milliken *et al.*, 2013). Fracture-like pores with jagged edges are also seen (Figures 14a, 14b), but they are relatively scarce and subordinate to microscale calcite- or bitumen-filled fractures which probably result from pore pressure increases related to petroleum generation (*cf.* Curtis *et al.*, 2013).

Overall, however, there is an average porosity *loss* of 7.9% between maturities of 0.53 and 0.89% Ro (11.8% to 3.9%; Table 2). Although hard to quantify, petrographic observations suggest that some of the porosity loss is due to what we term here chemically-enhanced mechanical compaction, seen for example in the collapse of algal bodies as a result of petroleum generation (Figure 6d). Bitumen phases may also fill porosity (Figures 9, 10). Since early mature samples have higher porosities and have the largest amounts of the extractable bitumen, we suggest that this early bitumen did not migrate but remained associated with kerogen (Sandvik *et al.*, 1992). In the peak oil window, continued generation resulted in micromigration, trapping and occlusion of both fracture and matrix porosity (Figures 9, 10); this can account for up to 3% porosity in the peak oil window (Table 3).

The average loss of TOC between 0.89 and 1.45% Ro is 1.0% (Table 2), corresponding to a potential porosity increase of approximately 2.4%, assuming a constant organic matter density and no mechanical compaction. This would result in an average gas window porosity of 6.3%, or 9.3% if we include the fraction of porosity potentially occluded by soluble bitumen in the oil window, compared to the measured average of 11.3% (which is remarkably similar to the average porosity of samples directly prior to petroleum generation; 11.8%; Table 2). The increased porosity coincides with the formation of isolated, spongy and complex organic matter-hosted meso- and macropores (Figures 15; 16), similar to those reported in several other gas-mature shales (Milliken *et al.*, 2012; 2013; 2015; Chalmers *et al*., 2012; Loucks *et al.*, 2012; Bernard *et al*., 2012; 2013). The lack of similar intraorganic porosity in immature and oil window samples suggests that it is the gasification process which generates the pores. However, the heterogeneity of the intraorganic porosity, even on a scale of a few microns (Figure 16) indicates that the processes which generate porosity in organic matter are quite complex. In our gas window sample, 65% of organic particles were not visibly porous in the SEM (although they are microporous; Rexer *et al*., 2014). Equally, at the scale observed in the BIB-SEM images, only 25% of total visible porosity is contained directly within organics, with the majority associated with minerals. Bernard *et al.'s* (2010; 2012) synchrotron-based studies suggested that macropores were specifically associated with pyrobitumen, rather than kerogen, asphaltene or NSO-rich bitumen, in both the Barnett and Posidonia Shale. Milliken *et al.'s* (2013) careful petrographic studies of gas-mature Marcellus shale came to a similar conclusion. Although it is difficult to be sure about the composition and origin of organic matter in SEM studies, the close association of porous and non-porous organic phases in gas-mature Posidonia shale, often directly adjacent to one another on a micron-scale, suggests that pyrobitumen-like, porous phases may have directly evolved from the neighbouring non-porous particles, were unable to migrate as a result of

capillary trapping and/or their high viscosity, and underwent further thermal cracking at higher temperatures. In this case, the visible pore structure likely marks a boundary between two different organic phases. This scenario may also apply to non-porous, arcuate terrestrial macerals, which are often rimmed with a porous organic phase.

Although we cannot be certain about the exact role of bitumen heterogeneity on the distribution of organic porosity, many authors point to the importance of hydrogen donor compounds such as asphaltenes or hydroaromatics as preventing cross-linking during cracking reactions (Behar and Pelet, 1988; Michelis, 1996; Schenk *et al.*, 1997) and therefore delaying the conversion and aromatization of the organic polymers (Lewan, 1997). On the other hand, Tiem *et al.* (2008) believed that although the absence of hydrogen donors may enhance cross-linking and reduce oil potential of an organic molecule, it will increase its gas potential at higher temperatures. It seems probable that the highly variable porosity development in organic phases relates to different chemophysical properties of the organic matter at the time of cracking, their association with unexpelled oil and their potential to release different hydrocarbon fractions, including wet gas and methane. Pyrolysis experiments on various coals have revealed different potential for porosity development depending on the maceral composition, their plastic properties as well as coal rank, with the viscosity and the advance in cross-linking shown to control the extent of the coal devolatilization (Alvarez *et al.*, 1997). The “bubble-like” nature of some pores may then represent the last step in gas exsolution from already polycondensed aromatic molecules (Tiem *et al.*, 2008), which were not able to release the pressure build up during gas generation but were viscous enough to prevent pore closure.

Although methane can be generated from high maturity kerogens in the laboratory (Guo *et al.*, 2009; Mahlstedt and Horsfield, 2012), it is still debatable whether residual kerogen itself can participate in development of organic porosity at gas window maturities. Bernard *et*

al. (2011) did not find any porosity in overmature kerogen, whereas Loucks *et al.* (2009) and Reed *et al*. (2014) suggest that porosity is developed within kerogen, including within the oil window. Our SEM micrographs show that in the HAD sample, approximately 65% of organic phases are not visibly porous. Sorption experiments by Rexer *et al.* (2014) showed that insoluble, bulk organic matter extracted from the overmature Posidonia shale is microporous – as is coal - but they did not separate kerogen from residual bitumen. It is plausible that the presence of internal microporosity within kerogen facilitates diffusive release of gas from kerogen and does not favour development of pores (Vanderbroucke and Largeau, 2007). Such microporosity may not occur in bitumen.

Recalling that 65% of organic matter particles in our gas window sample do not contain macropores, the macroporosity that we do observe in organic matter using SEM techniques cannot alone account for the substantial porosity increase observed from oil to gas window. Two other porosity sources seem plausible. Firstly, low pressure CO_2 and N_2 sorption experiments show that the volume of micro- and meso-porosity, unseen in our SEM studies, doubles or even trebles in Posidonia kerogen between 0.89 and 1.45% Ro (Rexer *et al*., 2014). Secondly, it is possible that kerogen shrinks as it matures from oil to gas window as a result of the loss of that fraction of oil which is generated within the kerogen and which is retained as sorbed oil (Sandvik *et al*., 1992). Swelling ratios of 1.1 to 1.7 were measured by Larsen and Li (1994) on Type II Albany kerogen using a set of solvents of different polarity, so that shrinkage upon loss of the oil is plausible and may be reflected as irregular pores both within organic matter and, more commonly, at the interface of organic and mineral matter.

5. Summary and Conclusions

1. Within our limited sample set, the porosity of Posidonia shales halves in the oil window compared to the immature shale and doubles in the gas window compared to

747 the oil mature shale. These changes can be explained by reference to (a) the primary
748 composition of the shales, (b) carbonate diagenesis, (c) compaction and (d) the
749 maturation, micro-migration, local trapping and gasification of heterogeneous organic
750 phases.

751 2. Biogenic calcite undergoes recrystallization, dissolution and reprecipitation reactions
752 throughout the maturity sequence; we suggest that the apparent retardation of
753 carbonate diagenesis, compared to chalk, is due to the higher clay contents of the
754 Posidonia shales, and also their likely oil-wet state.

755 3. Pores quantifiable by SEM (> ca. 50 nm) only account for 14-25% of total porosity.
756 At Ro = 0.5%, SEM-visible pores are associated mainly with biogenic calcite, with
757 essentially no macroporosity within the clay matrix or organic matter. At this
758 maturity, clays and organic matter are not visibly porous but nevertheless hold most
759 of the shale porosity.

760 4. Porosity loss in the oil window is due to (a) compaction, (b) carbonate cementation
761 and (c) perhaps the swelling of kerogen by retained oil. Porosity, especially in
762 macropores within microfossils, is also occluded by a range of bituminous phases,
763 some but not all of which can be extracted with organic solvents. Bitumen is also
764 observed in microfractures, probably related to increasing pressure in pores resulting
765 from petroleum generation. Some new pores are formed in the oil window, commonly
766 at organo-mineral interfaces and often associated with diagenetic calcite.

767 5. Increasing porosity into the gas window coincides with the formation of isolated,
768 spongy and complex meso- and macropores within organic matter, related to thermal
769 cracking and gas generation. Intraorganic porosity is highly heterogeneous; the
770 macroporosity of individual organic particles ranges from 0 - 40%, with 65% of
771 organic particles containing no macropores. The large variation in organic

772 macroporosity is considered to reflect both the differing chemophysical properties of
773 individual particles and the protection against compaction which a rigid mineral
774 matrix may afford softer organic phases. Microfossils thus play an important role in
775 the generation and retention of organic porosity since they are (a) bitumen traps and
776 (b) rigid.

777 6. The development of organic macroporosity cannot alone account for the porosity
778 increase observed from oil to gas window; an additional contribution must come from
779 the increased volume of micro- and meso-porosity. Furthermore, whilst intraorganic
780 pores are a very characteristic feature of gas window Posidonia shale, mineral-hosted
781 porosity is still the primary form of macroporosity, most commonly observed at the
782 organic-inorganic interface.

783

784

785 ## 7. References

786 ALVAREZ, D., BORREGO, A.G., MENENDEZ, R. 1997. Unbiased methods for the
787 morphological description of char structures. *Fuel*, **76**, 1241-1248.

788 APLIN, A.C., LARTER, S.R. 2005. Fluid Flow, Pore Pressure, Wettability, and Leakage
789 in Mudstone Cap Rocks. AAPG Special Bulletin**:** *AAPG Hedberg Series*, **2**, 1-12.

790 APLIN, A.C., MACQUAKER. H.S. 2010, Getting started in shales: American
791 Association of Petroleum Geologists/Datapages, Getting Started Series GS20.

792 BACHMANN, G.H., VOIGT, T., BAYER, U., VON EYNATTEN, H., LEGLER, B.,
793 LITTKE, R. (2008): Depositional history and sedimentary cycles in the Central European
794 Basin System. In: Littke,R., Bayer, U., Gajewski, D., Nelskamp, S. (Eds), Dynamics of

795 Complex Intracontinental Basins - The Central European Basin System, Springer-Verlag,
796 Berlin-Heidelberg, pp. 155-169.

797 BAKER, P.A., KASTNER, M., BYERLEE, J.D., LOCKNER, D.A., 1980. Pressure
798 solution and hydrothermal recrystallization of carbonate sediments—an experimental study.
799 *Marine Geology*, **38**, 185–203.

800 BEHAR, F., PELET, R. 1988. Hydrogen-Transfer Reactions in the Thermal Cracking of
801 Asphaltenes. *Energy & Fuels*, **2**, 259-264.

802 BEHAR, F., LORANT, F., LEWAN, M. 2008a. Role of NSO compounds during
803 primary cracking of a Type II kerogen and a Type III lignite. *Organic Geochemistry*, **39**, 1–
804 22.

805 BEHAR, F., LORANT, F., MAZEAS, L. 2008b. Elaboration of a new compositional
806 kinetic schema for oil cracking. *Organic Geochemistry*, **39**, 764–782.

807 BEHAR, F., ROY, S., JARVIE, D. 2010. Artificial maturation of a Type I kerogen in
808 closed system: Mass balance and kinetic modelling. *Organic Geochemistry*, **41**, 1235–1247.

809 BERNARD, S., HORSFIELD, B., SCHULTZ, H.M., SCHREIBER, A., WIRTH, R.,
810 TIEM, T.A.V., PERSSEN, F., KÖNITZER, S, VOLK, H., SHERWOOD, N., FUENTES, D.
811 2010. Multi-scale detection of organic and inorganic signatures provides insights into gas
812 shale properties and evolution. *Chemie der Erde*, **70**, 119-133.

813 BERNARD, S., HORSFIELD, B., SCHULTZ, H.M., WIRTH, R., SCHREIBER, A.,
814 SHERWOOD, N. 2011. Geochemical evolution of organic-rich shales with increasing
815 maturity: A STXM and TEM study of the Posidonia Shale (Lower Toarcian, northern
816 Germany). Marine and Petroleum Geology, 31, 70-89.

817 BERNARD, S., WIRTH, R., SCHREIBER, A., SCHULZ, H.-M., HORSFIELD, B.
818 2012. Formation of nanoporous pyrobitumen residues during maturation of the Barnett Shale
819 (Fort Worth Basin). *International Journal of Coal Geology*, **103**, 3–11.

820 BERNARD, S., WIRTH, R., SCHREIBER, A., BOWEN, L., APLIN, A.C., MATHIA,
821 E.J., SCHULZ, H.-M., HORSFIELD, B. 2013. FIB-SEM and TEM investigations of an
822 organic-rich shale maturation series from the lower Toarcian Posidonia Shale, Germany:
823 Nanoscale pore system and fluid-rock interactions. In: Camp, W., Diaz, E., Wawak, B.
824 (Eds.), Electron microscopy of shale hydrocarbon reservoirs, *AAPG memoir*, **102**, 53-66.

825 BOUR, I. MATTIOLI, E., PITTET, B. 2007. Nannofacies analysis as a tool to
826 reconstruct paleoenvironmental changes during the Early Toarcian anoxic event.
827 *Palaeogeography, Palaeoclimatology, Palaeoecology*, **249**, 58–79.

828 BRUNS, B., LITTKE, R., GASPARIK, M., van WEES, J.-D., NELSKAMP, S. 2014.
829 Thermal evolution and shale gas potential estimation of the Wealden and
830 Posidonia Shale in NW-Germany and the Netherlands: a 3D basin modeling
831 study. *Basin Research*, doi: 10.1111/bre.12096.

832 CHALMERS, G.R., BUSTIN, R.M., POWER, I.M. 2012. Characterization of gas shale
833 pore systems by porosimetry, pycnometry, surface area, and field emission scanning electron
834 microscopy/transmission electron microscopy image analyses: Examples from the Barnett,
835 Woodford, Haynesville, Marcellus, and Doig units. *American Association of Petroleum*
836 *Geologists Bulletin*, **96**, 1099-1119.

837 CLARKSON, C.R., SOLANO, N., BUSIN, R.M, BUSTIN, A.M.M., CHALMERS,
838 G.R.L., HE, L., MELNICHENKO, Y.B., RADLINSKI, A.P., BLACH, T.P. 2013. Pore

structure characterization of North American shale gas reservoirs using USANS/SANS, gas adsorption, and mercury intrusion. *Fuel*, **103**, 606–616.

CLEMENTZ, D.M. 1978. Effect of oil and bitumen saturation on source-rock pyrolysis. *American Association of Petroleum Geologists Bulletin*, **63**, 2227-2232.

CURTIS, M.E., SONDERGELD, C.H., RAI, C.S. 2013. Relationship between organic shale microstructure and hydrocarbon generation. SPE Unconventional Resources Conference-USA, 10-12 April 2013, The Woodlands, Texas, USA.

DESBOIS, G., URAI, J.L., KUKLA, P.A. 2009. Morphology of the pore space in claystones – evidence from BIB/FIB ion beam sectioning and cryo-SEM observations. *eEarth*, **4**, 15–22.

DIECKMANN, V., SCHENK, H.J., HORSFIELD, B., WELTE, D.H. 1988. Kinetics of petroleum generation and cracking by programmed-temperature closed-systempyrolysis of Toarcian Shales. *Fuel*, **77**, 23-31.

ESPITALIE, J., LAPORTE, J.L., MADEC, M., MARQUIS, F., LEPLAT, P., PAULET J., BOUTEFEU, A. 1977. Methode rapide de characterisation des roches meres, de leur potential petrolier et de leur degree d'evolution, *Rev. Inst. Franc. Pétrole*., **32**, 23-42

FABRICIUS, I.L. 2003. How burial diagenesis of chalk sediments controls sonic velocity and porosity. *American Association of Petroleum Geologists Bulletin*, **87**, 1755 – 1778.

FABRICIUS, I.L., GOMMESEN, L., KROGSBØLL, A., OLSEN, D. 2008. Chalk porosity and sonic velocity versus burial depth: Influence of fluid pressure, hydrocarbons, and mineralogy. *American Association of Petroleum Geologists Bulletin*, **92**, 201-223.

FISHMAN, N.S., HACKLEY, P.C., LOWERS, H.A., HILL, R.J., EGENHOFF, S.O., EBERL, D.D., BLUM, A.E. 2012. The nature of porosity in organic-rich mudstones of the Upper Jurassic Kimmeridge Clay Formation, North Sea, offshore United Kingdom. *International Journal of Coal Geology*, **103**, 32–50.

GUO, L., XIANMING, X, HUI, T., ZHIGUANG, S. 2009. Distinguishing gases derived from oil cracking and kerogen maturation: Insights from laboratory pyrolysis experiments. *Organic Geochemistry*, **40**, 1074–1084.

HEASLEY, E.C., WORDEN, R.H., HENDRY, J.P. 2000. Cement distribution in a carbonate reservoir: Recognition of a paleo-oil–water contact and its relationship to reservoir quality in the Humbly Grove field, onshore, United Kingdom. *Marine and Petroleum Geology*, **17**, 639–654.

HAMMES, U., FRÉBOURG, G. 2012. Haynesville and Bossier mudrocks: A facies and sequence stratigraphic investigation, East Texas and Louisiana, USA. *Marine and Petroleum Geology*, **31**, 8-26.

HEATH, J.E., DEWERS, T.A., McPHERSON, B.J.O.L., PETRUSAK, R., CHIDSEY, Jr. T.C., RINEHART, A.J., MOZLEY, P.S. 2011. Pore networks in continental and marine mudstones: Characteristics and controls on sealing behaviour. *Geosphere*, **7**, 429–454.

HESSE, R. 1990. Origin of chert: diagenesis of biogenic siliceous sediments. In: McIlreath, I.A., Morrow, D.W. (Eds.), Diagenesis Geoscience, Geological Association of Canada, St. John's, Newfoundland, Canada, Reprint Ser., **4**, 227-251.

HORSFIELD, B., SCHENK, H.J., MILLS, N., WELTE, D.H. 1992. An investigation of the in-reservoir conversion of oil to gas: compositional and kinetic findings from closed-system programmed-temperature pyrolysis. *Organic Geochemistry*, **19**, 191-204.

884 HORSFIELD, B., LITTKE, R., MANN, U., BERNARD, S., TIEM, A.T.V., Di PRIMIO,
885 R., SCHULZ, H.-M. 2010. Shale Gas in the Posidonia Shale, Hils Area, Germany. American
886 Association of Petroleum Geologists Annual Convention, April 11-14, 2010, New Orleans,
887 LA, USA.

888 HOUBEN, M.E., DESBOIS, G., URAI, J.L. 2013. Pore morphology and distribution in
889 the Shaly facies of Opalinus Clay (Mont Terri, Switzerland): Insights from representative 2D
890 BIB-SEM investigations on mm to nm scale. *Applied Clay Science*, **71**, 82-97.

891 HWANG, R.J., TEERMAN, S.C., CARLSON, R.M. 1998. Geochemical comparison of
892 reservoir solid bitumens with diverse origins. *Organic Geochemistry*, **29**, 505-517.

893 JARVIE, D.M., HILL, R.J., RUBLE, T.E., POLLASTRO, R.M., 2007. Unconventional
894 shale-gas systems: the Mississippian Barnett Shale of north-central Texas as one model for
895 thermogenic shale gas assessment. *American Association of Petroleum Geologists Bulletin*,
896 **91**, 475–499.

897 KIETZMANN, D.A., MARTÍN-CHIVALET, J., PALMA, R.M., LÓPEZ-GÓMEZ, J.,
898 LESCANO, M. 2011. Evidence of precessional and eccentricity orbital cycles in a Tithonian
899 source rock: The mid-outer carbonate ramp of the Vaca Muerta Formation, northern Neuquén
900 Basin, Argentina. *American Association of Petroleum Geologists Bulletin*, **95**, 1459-1474.

901 KLAVER, J., DESBOIS, G., URAI, J.L., LITTKE, R. 2012. BIB-SEM study of the pore
902 space morphology in early mature Posidonia Shale from the Hils area, Germany.
903 *International Journal of Coal Geology*, **103**, 12-25.

904 KLAVER, J., DESBOIS, G., LITTKE, R., URAI, J.L. 2015. BIB-SEM characterization
905 of pore space morphology and distribution in postmature to overmature samples from the
906 Haynesville and Bossier Shales. *Marine and Petroleum Geology*, **59**, 451-466.

907 LANDIS, C.R., CASTAÑO, J.R. 1995. Maturation and bulk chemical properties of a
908 suite of solid hydrocarbons. *Organic Geochemistry*, **22**, 137-149.

909 LARSEN, J.W., LI, S. 1994. Solvent swelling studies of Green River kerogen. Energy &
910 Fuels, **8**, 932-936.

911 LEWAN, M.D., 1997. Experiments on the role of water in petroleum formation.
912 *Geochimica et Cosmochirnica Acta*, **61**, 3691-3723.

913 LEYTHAEUSER, D., LITTKE, R., RADKE, M., SCHAEFER, R.G. 1988. Geochemical
914 effects of petroleum migration and expulsion from Toarcian source rocks in the Hils syncline
915 area, NW-Germany. *Organic Geochemistry*, **13**, 489-502.

916 LIANG, C., JIANG, Z., ZHANG, C., GUO, L., YANG, Y., LI., J. 2014. The shale
917 characteristics and shale gas exploration prospects of the Lower Silurian Longmaxi shale,
918 Sichuan Basin, South China. *Journal of Natural Gas Science and Engineering*, **21**, 636-648.

919 LITTKE, R., BAKER, D.R., RULLKÖTTER, J. 1987 Deposition of petroleum source
920 rocks. In: Welte, D.H., Horsfield, B., Baker, D.R. (Eds.). Petroleum and Basin Evolution:
921 Insights from petroleum geochemistry, geology and basin modelling. Springer-Verlag,
922 Heidelberg, pp. 271-333.

923 LITTKE, R., BAKER, D.R., LEYTHAEUSER, D., RULLKÖTTER, J. 1991. Keys to the
924 depositional history of the Posidonia Shale (Toarcian) in the Hils Syncline, northern
925 Germany. In: Tyson, R.V., Pearson, T.H. (Eds.) Modern and ancient continental shelf anoxia.
926 *Geological Society Special Publication*, **58**, 311-333.

927 LOMANDO, A.J. 1992. The influence of solid reservoir bitumen on reservoir quality.
928 *American Association of Petroleum Geologists Bulletin*, **76**, 1137–1152.

LOUCKS, R.G., REED, R.M., RUPPEL, S.C., JARVIE, D.M. 2009. Morphology, genesis and distribution of nanometer-scale pores in siliceous mudstones of the Mississippian Barnett Shale. *Journal of Sedimentary Research*, **79**, 848–861.

LOUCKS, R.G., REED, R.M., RUPPEL, S.C., HAMMES, U. 2012. Spectrum of pore types and networks in mudrocks and a descriptive classification for matrix-related mudrock pores. *American Association of Petroleum Geologists Bulletin*, **96**, 1071-1098.

LOUCKS, R.G., REED, R.M. 2014. Scanning-Electron-Microscope petrographic evidence for distinguishing organic-matter pores associated with depositional organic matter versus migrated organic matter in mudrocks. *GCAGS Journal*, **3**, 51-60.

MACKENZIE, A.S., LEYTHAEUSER, D., ALTEBÄUMER, F.-J., DISKO, U., RULLKÖTTER, J. 1988. Molecular measurements of maturity for Lias 6 shales in N.W. Germany. *Geochimica et Cosmochimica Acta*, **52**, 1145-1154.

MACQUAKER, J.H.S., TAYLOR, K.G., GAWTHORPE, R.L. 2007. High-resolution facies analyses of mudstones: implications for paleoenvironmental and sequence stratigraphic interpretations of offshore ancient mud-dominated successions. *Journal of Sedimentary Research*, **77**, 324–339.

MACQUAKER, J.H.S., TAYLOR, K.G., KELLER, M., POLYA, D. 2014. Compositional controls on early diagenetic pathways in fine-grained sedimentary rocks: Implications for predicting unconventional reservoir attributes of mudstones. *American Association of Petroleum Geologists Bulletin*, **98**, 587–603.

MAHLSTEDT, N., HORSFIELD, B. 2012 Metagenetic methane generation in gas shales I. Screening protocols using immature samples. Marine and Petroleum Geology, **31**, 27-42.

951 MALLON, A.J., SWARBRICK, R.E. 2002. A compaction trend for non-reservoir North
952 Sea Chalk. *Marine and Petroleum Geology*, **19**, 527-539.

953 MANN, U., MÜLLER, P.J. 1988. Source rock evaluation by well log analysis (Lower
954 Toarcian, Hils syncline). *Organic Geochemistry*, **13**, 109-119.

955 MASTALERZ, M., GLIKSON, M. 2000. In-situ analysis of solid bitumen in coal:
956 examples from the Bowen Basin and the Illinois Basin. *International Journal of Coal*
957 *Geology*, **42**, 207–220.

958 McHARGUE, T.R., PRICE, R.C. 2006. Dolomite from clay in argillaceous or shale-
959 associated marine carbonates. *Journal of Sedimentary Research*, **52**, 873-886.

960 MICHELIS, R., LANGLOIS, E., RUAU, O., MANSUY, L., ELIE, M., LANDAIS, P.
961 1996. Evolution of asphaltenes during artificial maturation: A record of the chemical
962 processes. *Energy & Fuels*, **10**, 39-48.

963 MILLIKEN, K.L., ESCH, W. L., REED, R. M., ZHANG, T. 2012. Grain assemblages
964 and strong diagenetic overprinting in siliceous mudrocks, Barnett Shale (Mississippian), Fort
965 Worth Basin, Texas. *American Association of Petroleum Geologists Bulletin*, **96**, 1553-1578.

966 MILLIKEN, K.L., RUDNICKI, M., AWWILER, D.N., ZHANG, T. 2013. Organic
967 matter–hosted pore system, Marcellus Formation (Devonian), Pennsylvania. *American*
968 *Association of Petroleum Geologists Bulletin*, **97**, 177-200.

969 MUÑOZ, Y.A., LITTTKE, R., BRIX, M.R. 2007. Fluid systems and basin evolution of
970 the western Lower Saxony Basin, Germany. *Geofluids*, **7**, 335–355.

971 OKIONGBO, K.S., APLIN, A.C., LARTER, S.R. 2005. Changes in Type II kerogen
972 density as a function of maturity: Evidence from the Kimmeridge Clay Formation. *Energy &*
973 *Fuels*, **19**, 2495-2499.

974 PASSEY, Q. R., BOHACS, K. M., ESCH, W. L., KLIMENTIDISS, R., SINHA, S.
975 2010. From Oil-Prone Source Rock to Gas-Producing Shale Reservoir – Geologic and
976 petrophysical characterization of unconventional shale-gas reservoirs. *Proceedings of the*
977 *North American Unconventional Gas Conference and Exhibition. Society of Petroleum*
978 *Engineers*, Paper 131350, 29p.

979 POMMER, M., MILLIKEN, K. 2015. Pore types and pore-size distributions across
980 thermal maturity, Eagle Ford Formation, southern Texas. *American Association of Petroleum*
981 *Geologists Bulletin*, **99**, 1713-1744.

982 POTTER, P.E., MAYNARD, J.B., DEPETRIS, P.J. 2005. Mud and Mudstones:
983 Introduction and overview. Springer-Verlag, Berlin, pp. 297.

984 RADKE, M., VRIEND, S.P., SCHAEFER, R.G. 2001. Geochemical characterization of
985 Lower Toarcian source rocks from NW Germany: interpretation of aromatic and saturated
986 hydrocarbons in relation to depositional environment and maturation effects. *Journal of*
987 *Petroleum Geology*, **24**, 287-307.

988 REED, R.M., LOUCKS, R.G., RUPPEL, S.C. 2014. Comment on "Formation of
989 nanoporous pyrobitumen residues during maturation of the Barnett Shale (Fort Worth
990 Basin)". *International Journal of Coal Geology*, **127**, 114-115.

991 REXER, T.F.T., BENHAM, M.J., APLIN, A.C., THOMAS, K.M. 2013. Methane
992 adsorption on shale under simulated geological temperature and pressure conditions. *Energy*
993 *& Fuels*, **27**, 3099-3109.

994 REXER, T.F.T, MATHIA, E.J., APLIN, A.C., THOMAS, K.M. 2014. High-Pressure
995 Methane Adsorption and Characterization of Pores in Posidonia Shales and Isolated
996 Kerogens. *Energy & Fuels*, **28**, 2886-2901.

997 RODUIT. 2008. JMicroVision: Image analysis toolbox for measuring and quantifying
998 components of high-definition images. Version 1.2.7. Software available for free download at
999 http://www.jmicrovision.com/ accessed August, 2011.

1000 ROSS, D.J.K, BUSTIN. 2009. The importance of shale composition and pore structure
1001 upon gas storage potential of shale gas reservoirs. *Marine and Petroleum Geology*, **26**, 916–
1002 927.

1003 RÖHL, H.J., SCHMID- RÖHL, A., OSCHMANN, W., FRIMMEL, A., SCHWARK, L.
1004 2001. The Posidonia Shale (Lower Toarcian) of SW-Germany: an oxygen-depleted
1005 ecosystem controlled by sea level and palaeoclimate. *Palaeogeography, Palaeoclimatology,*
1006 *Palaeoecology*, **165**, 27–52.

1007 RÖHL, H.J., SCHMID- RÖHL, A. 2005. Lower Toarcian (Upper Liassic) black shales
1008 of the Central European epicontinental basin: a sequence stratigraphic case study from the
1009 SW German Posidonia Shale. In: HARRIS, N. B. (Ed.), The deposition of organic carbon-
1010 rich sediments: Models, mechanisms, and consequences: Society for Sedimentary Geology
1011 Special Publication, **82**, 165-189.

1012 RULLKÖTTER, J., LEYTHAEUSER, D., HORSFIELD, B., LITTKE, R., MANN, U.,
1013 MÜLLER, P.J., RADKE, M., SCHAEFER, H.-J., SCHWOCHAU, K., WITTE, E.G.,
1014 WELTE, D.H. 1988. Organic matter maturation under the influence of a deep intrusive heat
1015 source: A natural experiment for quantitation of hydrocarbon generation and expulsion from

a petroleum source rock (Toarcian shale, northern Germany). *Organic Geochemistry*, **13**, 847-856.

SANDVIK, E.I., YOUNG, W.A., CURRY, D.J. 1992. Expulsion from hydrocarbon sources: the role of organic absorption. *Organic Geochemistry*, **19**, 77-87.

SCHAEFER, R.G., LITTKE, R. 1988. Maturity-related compositional changes in the low-molecular-weight hydrocarbon fraction of Toarcian shales. *Organic Geochemistry*, **13**, 887-892.

SCHENK, H.J., DI PRIMIO, R., HORSFIELD, B. 1997. The conversion of oil into gas in petroleum reservoirs. Part 1: Comparative kinetic investigation of gas generation from crude oils of lacustrine, marine and fluviodeltaic origin by programmed-temperature closed-system pyrolysis. *Organic Geochemistry*, **26**, 467-481.

SCHIEBER, J. 1999. Distribution and deposition of mudstone facies in the Upper Devonian Sonyea Group of New York. *Journal of Sedimentary Research*, **69**, 909-925.

SCHOLLE, P. A. 1977. Chalk diagenesis and its relation to petroleum exploration: oil from chalks, a modern miracle? *American Association of Petroleum Geologists Bulletin*, **61**, 982-1009.

SCHOLLE, P. A., HALLEY, R. B. 1985. Burial diagenesis: out of sight, out of mind! In*:* Schneidermann, N., Harris, P.M. (Eds.), Carbonate Cements: Tulsa, OK, *SEPM Special Publication*, **36**, 309-334.

SLATT, R.M., O'BRIEN, N.R. 2011. Pore types in the Barnett and Woodford gas shales: Contribution to understanding gas storage and migration pathways in fine-grained rocks. *AAPG Bulletin*, **95**, 2017–2030.

TANG, X., ZHANG, J., WANG, X., YU, B., DING, W., XIONG, J., YANG, Y., WANG, L., YANG, C. 2014. Shale characteristics in the Southeastern Ordos Basin, China: Implications for hydrocarbon accumulation conditions and the potential of continental shales. *International Journal of Coal Geology*, **128-129**, 32-46.

TAO, S., WANG, Y., TANG, D., WU, D., XU, H., HE, W. 2012. Organic petrology of Fukang Permian Lucaogou Formation oil shales at the northern foot of Bogda Mountain, Junggar Basin, China. *International Journal of Coal Geology*, **99**, 27–34.

TIEM, V.T., HORSFIELD, B., SYKES, R. 2008. Influence of in-situ bitumen on the generation of gas and oil in New Zealand coals. *Organic Geochemistry*, **39**, 1606–1619.

TISSOT, B.P., WELTE, D.H. 1984. Petroleum formation and occurrence. Springer-Verlag, New York, pp. 699.

TRABUCHO-ALEXANDRE, J., DIRKX, R., VELD, H., KLAVER, G., De BOER, P.L. 2012. Toarcian black shales in the Dutch Central Graben: record of energetic, variable depositional conditions during an Oceanic Anoxic Event. *Journal of Sedimentary Research*, **82**, 104–120.

TYSON, R.V. 1995. Sedimentary Organic Matter: Organic facies and palynofacies. Chapman & Hall, London, pp.615.

VANDENBROUCKE, M.., BEHAR, F., SAN TORCUATO, A., RULLKÖTER, J. 1993. Kerogen maturation in a reference kerogen Type II series: the Toarcian shales of the Hils syncline, NW Germany. *Organic Geochemistry*, **20**, 961-972.

VANDENBROUCKE, M.., LARGEAU, C. 2007. Kerogen origin, evolution and structure. *Organic Geochemistry*, **38**, 719–833.

VAN DUIN, A.C.T., LARTER, S.R. 2001. A computational chemical study of penetration and displacement of water films near mineral surfaces, Geochemical Transactions 6.

WELTE, D.H., HORSFIELD, B., BAKER, D.R. (Eds.). 1997. Petroleum and Basin Evolution: Insights from petroleum geochemistry, geology and basin modelling. Springer-Verlag, Berlin, Heidelberg, New York, London, Paris, Tokyo, Hong Kong, pp.535.

WILHELMS, A., LARTER, S.R., LEYTHAEUSER, D., DYPVIK, H. 1990. Recognition and quantification of the effects of primary migration in a Jurassic clastic source-rock from the Norwegian. *Organic Geochemistry*, **16**, 103-113.

WORDEN, R.H., OXTOBY, N.H., SMALLEY, P.C. 1998. Can oil emplacement prevent quartz cementation in sandstones? *Petroleum Geoscience*, **4**, 129–137.

8. Acknowledgements

This work was supported by the Gas Shales in Europe project funded by Bayerngas, ExxonMobil, GdFSuez, Marathon, Repsol, Schlumberger, Statoil, Total, Vermilion and Wintershall. Bruce Hart and Kitty Milliken are thanked for their highly constructive reviews.

List of Figures

Figure 1. Location of Hils syncline, Northern Germany and three boreholes: Wickensen (WIC; R_o 0.53%), Harderode (HAR; 0.89%) and Haddessen (HAD, 1.45%) (after Mann and Müller (1988) and Horsfield *et al*. (2010)). b) Lithological profile of the Posidonia Shale from the three boreholes with a marlstone unit (I) and two calcareous shale units (II and III); red dots represent sample locations (after Littke *et al*. (1991)).

Figure 2. Scans of polished thin sections. The bedding plane is horizontal. Vertical arrows denote thickness of distinguishable laminae. a) (WIC 7129): Horizontal lamination marked by the alternation of more calcite- and clay-rich horizons. The thickness of individual laminae reaches up to 3 mm. b) (WIC 7153): Lenticular lamination with large faecal pellets up to 0.6 mm. Faecal-pellet diluted horizons alternate with horizons with higher proportions of clay (darker lamina). c) (HAD 7101): Alternating dark and light laminae, reflecting different amounts of carbonate and clay are still visible in this higher maturity shale. d) (HAD 7119): Any original lamination has been lost in this high maturity marlstone sample. D – dark, clay-rich lamina, L – light, carbonate-rich lamina, FP – faecal pellet, T – terrestrial organic matter.

Figure 3. Plane-polarized-light optical micrographs, Wickensen. a) (WIC 7129): Flattened, compacted algal bodies (green arrow) and faecal pellets (red arrow) constitute well-oriented components in the fabric of the calcareous clay-shale. b) (WIC 7139): Microlamination marked by different amounts of matrix calcite. Ligher units (centre and bottom) are relatively enriched in calcite and impoverished in clay as compared to darker units (top). Large faecal pellets (> 500 µm), visible at the top, are scarce in the upper, clay-rich Posidonia unit. c) (WIC 7145): A layer of silt-sized carbonate grains separates two laminae. Shale below the silt layer has larger faecal pellets (red arrow) and is lighter in plane-polarized light. d) (WIC

7151): An example of lenticular microlamination in a sample from the marlstone unit. The bright horizontal lenses (red arrow) are composed of well-defined faecal pellets. Flattened, organic-rich clay aggregates are marked with a green arrow. e) (WIC 7153): Well-developed, lenticular lamination due to the presence of ubiquitous faecal pellets (red arrow). Small particles of woody organic matter are disseminated in the shale matrix (orange arrow). f) (WIC 7153): Details of the lenticular lamination. Large faecal pellets, up to 500 µm in length (red arrow), alternate with brown organo-clay aggregates (green arrow). A woody organic particle is marked with an orange arrow.

Figure 4. Plane-polarized-light optical micrographs, Harderode. a) (HAR 7038): Lamination in this calcareous clay-shale is due to presence of layers containing differing amounts of quartz and authigenic pyrite. An uneven surface below the bottom silt layer may be erosive in origin. b) (HAR 7046): Preserved original lamination is picked out by a layer of silt-size quartz grains in the middle of the image. c) (HAR 7060): Carbonate cement, most likely precipitated within an algal cyst (red arrow). Green arrow denotes authigenic pyrite filling a small bivalve. d) (HAR 7060): Carbonates often show rhombohedral shapes (red arrow), suggesting in-situ precipitation. e) Large foraminifer test with intraparticle carbonate cement. f) (HAR 7070): Sub- and euhedral carbonate crystals lining a small fracture (red arrow).

Figure 5. Plane-polarized-light optical micrographs, Haddessen. a) (HAD 7083): Small-scale heterogeneity of the calcareous clay-shale is imparted by the presence of flattened and oval faecal pellets (red arrows). The unit at the top has also more silty material (carbonates and quartz), and more pyrite (green arrow). b) (HAD 7101): Diagenetic carbonates are concentrated in specific layers. c) (HAD 7101): Micrograph of an area within (b). Flattened carbonate aggregates are composed of sparry calcite cement (green arrow) or show

microcrystalline texture in faecal pellets (red arrow). Matrix carbonates alternate with aggregates enriched in clays and organic matter on a < 100 µm scale. d) (HAD 7101): Microlamination marked by different concentrations of faecal pellets. A lamina in the centre is more enriched in faecal pellets (red arrows) than the unit at the top of the image. e) (HAD 7110): Diagenetically altered matrix of the calcareous clay-shale, with large faecal pellets (red arrow) and discrete carbonate cements (green arrow). Carbonate phases are disseminated in the more clay-rich shale. f) (HAD 7119): In this carbonate-rich mudstone, the shale matrix is dominated by a network of compacted faecal pellets (red arrows).

Figure 6. Backscattered electron micrographs, Wickensen and Harderode. The bedding plane in all images is horizontal. a) (WIC 7129): Microlaminated calcareous clay-shale (light lamina) with alternating faecal pellet-rich (red arrow) and clay-rich layers (green arrows). Visible organic matter is mostly associated with the clay-rich areas. Silt-sized quartz and pyrite are common, widely disseminated in the matrix. b) (WIC 7129): Details of the nannofossil enrichment in a dark lamina of the calcareous shale. Biogenic calcite is surrounded by clays. Coccoliths are mostly broken and authigenic overgrowths, if present, are very subtle, resulting in more equant edges of coccoliths (red arrows). Organic matter (green arrow) forms elongated laminae. c) (WIC 7155): Nannofossil-rich pellets in a marlstone sample with ubiquitous inter- and intragranular cement and partially recrystallized nannofossil structures. Recrystallized biogenic calcite fragments are suggested by the presence of faceted calcite crystals (red arrows) coexisting with unmodified fossil structures. Clay laminae (green arrow) are volumetrically less abundant than in the calcareous shale. d) (HAR 7046): Calcareous clay-shale at peak oil window maturity, at low magnification. Organic structures, ubiquitous at lower maturities, have collapsed (green arrows). e) (HAR

7046): Calcite cement precipitated in an algal cyst, locally preventing compaction. f) (HAR 7046): A lamina of detrital quartz with intergranular quartz, pyrite and kaolinite cement.

Figure 7. Backscattered electron micrographs, Harderode and Haddessen. The bedding plane in all images is horizontal except for image (f). a) (HAR 7060): A foraminifer with intraparticle calcite and pyrite cement (red arrow) filling original intrafossil pores. Above, a quartz-rich lamina with authigenic quartz cementing detrital grains (green arrow). The biogenic material in faecal pellets (orange arrow) shows signs of local cement precipitation, interlocking biogenic grains. b) (HAR 7070): Diagenetically-altered faecal pellet (centre) showing inter- and intragranular authigenic calcite textures. Authigenic, rhombohedral dolomite cement marked with a green arrow. c) (HAD 7083): Gas window shale. Authigenic pyrite forms small euhedra, oval framboids or directly replaces biogenic calcite (red arrow) and quartz (green arrow). Small authigenic calcite (microcarbs) grains are ubiquitous in the matrix. d) (HAD 7083): Calcareous shale showing evidence of recrystallized calcite, with faceted calcite crystals replacing coccoliths (red arrows) and intraparticle cement filling intrafossil canals (green arrow). e) (HAD 7083): Interlocking calcite texture within a fossiliferous aggregate, dominated by faceted authigenic calcite. Unaltered coccoliths are very rare (red arrow). f) (HAD 7115): Large zone of calcite cement with authigenic kaolinite in the centre. This large calcite zone may also be a now-unrecognizable fossil fragment. Bedding plane is marked with a dashed line.

Figure 8. SEM-EDX-ray maps displaying microlamination at all maturities (a) WIC 7129, b) HAR 7060, c) HAD 7110). The microlamination is marked by the alternating pattern of carbonate-rich (blue) and clay-rich (green) laminae, and in the lower maturity samples, also organic wisps (pink). The bedding plane in all images is horizontal.

Figure 9. Paired oil immersion (left) and reflected light (right) micrographs. Horizontal scale bar denotes 50 µm. Dashed line indicates direction of bedding plane. a, b) (WIC 7129): Wisps and oval bodies of algal cysts (A_T Tasmanales, A_L Leiosphaeridales) constitute the most prominent organic components. Other macerals include: unidentified alginates (A), bituminite (B), vitrinite (V), inertinite (I). Strong fluorescence of the matrix is due to the presence of the matrix bituminite. The contrast in this micrograph has been subdued due to strong yellow fluorescence. c ,d) (HAR 7060): Algal bodies are mostly collapsed (A_L). Matrix bituminite shows much weaker fluorescence. Solid bitumen (B_S) is present in the matrix, concentrated in fossiliferous zones. An inset in d) shows a fragment of a fracture filled with solid bitumen and authigenic carbonates (C). e, f) (HAD 7110): No alginate is present and the matrix is only marginally fluorescent. Solid bitumen (B_S) forms a dense network in the shale matrix and within fossiliferous units.

Figure 10. Secondary Electron micrographs of BIB-polished samples after solvent extraction. a) (HAR 7060): Non-extractable solid bitumen (dark) in this oil window sample fills pore space between faceted calcite crystals (black arrows) in a fossiliferous domain. b) (HAD 7110): In this gas window sample, non-extractable and porous solid bitumen (with pores < 100 nm) fills the pore space between pyrite crystallites in a framboid.

Figure 11. Point counted image porosity in % (a) and as a fraction of total porosity (b).

Figure 12. Ternary diagram showing distribution of visible SEM porosity (pixel size 15 nm) in WIC 7129 (0.53% Ro) (black circle), HAR 7060 (0.89% Ro) (red circle) and HAD 7110 (1.45% Ro) (green circle).

Figure 13. FIB-SEM and BIB-SEM micrographs, Wickensen. Bedding is perpendicular to the plane of view. a) Intraparticle pores within a coccolith canal; b) Intraparticle pores in a fragment of Schizophaerella; c) Intraparticle pores in a compacted, crushed faecal pellet; d) Intraparticle pores in a faecal pellet with ubiquitous calcite cement; e) Intraparticle pores lined with the organic material in a fragment of Schizophaerella; f) Intraparticle pore in clay, with authigenic pyrite precipitated between clay platelets; g) Intraparticle pore within a calcite-cemented pyrite framboid; h) Intraparticle calcite dissolution pore; i) Interparticle pore associated with faceted authigenic calcite and recrystallized biogenic debris; j) Interparticle pore associated with biogenc calcite; k) Organic matter-associated pores at the interface with the mineral matrix; l) Organic matter-hosted pore within an algal body. Cal – calcite, Dol – dolomite, Py – pyrite, Qtz – quartz, OM – organic matter.

Figure 14. FIB-SEM and BIB-SEM micrographs, Harderode. Bedding is perpendicular to the view plane. a) Fracture within organic matter (OM) extending into the organic-mineral interface; b) Fracture at the interface of OM and calcite; c) Interparticle pore at the interface of OM and calcite; d) Interparticle pores from the OM interface; e) Interparticle pores at the interface of OM and authigenic calcite crystals; f) Interparticle, crack-like pore from the interface of OM and diagenetic calcite; g) Interparticle pore associated with matrix dolomite and calcite; h) Open fracture-like pore within clay; i) Intraparticle, cleavage-associated pore in mica; j) Intraparticle pores within a pyrite framboid; k) Intraparticle pore formed due to dissolution of dolomite ; l) Intraparticle pore associated with authigenic calcite. Cal – calcite, Dol – dolomite, M – mica, Py – pyrite, Qtz – quartz, OM – organic matter.

Figure 15. FIB-SEM and BIB-SEM micrographs, Haddessen. Bedding is perpendicular to the view plane. a) Discrete, bubble-like pores within an organic matter; b) Spongy organic matter-hosted pores, visibly interconnected and grouped; c) Pendular, rounded organic matter-associated pores; discrete pores are also present; d) Complex organic matter-hosted pore from the interface with the mineral matrix; e) Complex organic matter-hosted pore extending into the organic particle, occupying the interface with the mineral matrix in the 3D space; f) Organic matter-hosted pores bordering a terrestrial organic maceral; g) Partly compacted pores within a terrestrial organic maceral; h) Interparticle pore at the interface of organic matter with diagenetic calcite and clays; i) Interparticle pores between clusters of pyrite framboids and quartz. Cal – calcite, Py – pyrite, Qtz – quartz, OM – organic matter.

Figure 16. FIB-SEM and BIB-SEM micrographs, Haddessen. Bedding is perpendicular to the view plane. a) Interparticle pore between clay aggregates; b) Interparticle pore between faceted calcite crystals. The pore is lined with organics and thus resembles organic matter-hosted porosity; c) Interparticle pores at the interface of OM and diagenetic calcite. Note discrete and spongy pores within the organic phase; d) Intraparticle pores in a fossil fragment; e) Intraparticle pores in a pyrite framboid. Pyrite-associated pores coexist with complex and spongy organic matter-hosted pores; f) Intra-clay pores, partly filled with OM and pyrite; g) Intraparticle pores within clays evolved due to precipitation of diagenetic pyrite; h) Intraparticle dolomite-dissolution pore; i) Intraparticle pores within calcite cement. Cal – calcite, Dol – dolomite, Py – pyrite, OM – organic matter.

1247 **Table 1.** TOC-normalized mineralogical composition (wt.%) for WIC (Ro 0.53%), HAR (Ro 0.89%)

1248 and HAD (Ro 1.45%). n.d. = not detected

	7129	WIC 7125	WIC 7145	WIC 7147	WIC 7155	HAR 7039	7046	7060	HAR 7070	HAD 7083	HAD 7099	7110	HAD 7119
Quartz	12.4	15.1	11.8	14.0	7.8	14.6	16.4	12.2	10.8	11.0	14.8	14.1	7.6
Plagioclase	1.0	0.2	0.9	0.6	1.3	1.9	2.0	2.6	3.7	2.4	2.8	3.2	4.5
K-Feldspar	0.7	0.0	0.0	0.0	0.0	0.5	0.4	0.4	0.5	0.5	0.1	0.7	0.6
Calcite	32.4	35.8	41.5	38.1	50.0	40.1	39.5	28.7	42.2	49.0	36.8	28.5	46.3
Dolomite	0.3	0.0	0.3	0.2	0.5	0.6	1.0	6.0	2.0	0.6	1.7	3.7	2.5
Siderite/ Ankerite	0.4	0.0	0.8	1.8	0.5	0.2	0.3	0.3	0.3	0.1	0.8	0.4	0.6
Aragonite	n.d.	n.d.	1.2	n.d.	1.2	n.d.	n.d.	n.d.	n.d.	n.d.	0.6	n.d.	1.4
Pyrite	4.8	4.5	3.5	3.7	4.9	5.2	4.8	8.6	5.2	6.9	4.6	6.6	4.2
Marcasite	0.7	n.d.	n.d.	n.d.	n.d.	0.6	0.2	0.9	1.2	n.d.	n.d.	0.2	n.d.
Anatase	0.3	0.1	n.d.	0.1	n.d.	0.3	0.2	0.2	0.3	0.2	n.d.	0.4	n.d.
Muscovite	2.3	2.2	0.0	1.2	0.1	2.9	2.8	3.5	3.0	2.4	1.2	4.4	0.0
Illite + I/S	21.7	22.0	20.0	25.4	17.5	17.0	18.9	24.7	18.3	13.2	22.1	23.5	18.1
Kaolinite	10.4	6.0	4.5	7.1	2.0	8.2	6.8	6.2	4.0	6.0	3.6	8.1	1.0
Dickite	n.d.	n.d.	1.1	n.d.	0.9	n.d.	n.d.	n.d.	n.d.	n.d.	1.2	n.d.	0.0
Chlorite	n.d.	0.4	1.8	0.2	1.6	n.d.	n.d.	n.d.	n.d.	0.0	0.6	n.d.	2.5
Gypsium	n.d.	0.3	2.0	0.4	2.2	n.d.	n.d.	n.d.	n.d.	0.4	1.7	n.d.	3.5
Halite	n.d.	0.1	n.d.	n.d.	n.d.	n.d.	n.d.	n.d.	n.d.	0.1	n.d.	n.d.	n.d.
TOC	12.6	13.3	10.9	7.3	9.7	7.9	6.8	5.8	8.7	6.4	7.4	6.4	7.2
Total	100	100	100	100	100	100	100	100	100	100	100	100	100

1249

1250

1251 **Table 2.** Leco, Rock-Eval, grain density and total porosity results for selected Posidonia samples from

1252 wells WIC (Ro 0.53%), HAR (Ro 0.89%) and HAD (Ro 1.45%).

Sample	TOC (%)	S1 (mgHC/g)	S2 (mgHC/g)	HI (mgHC/gC)	T_{max} (°C)	Grain Density (g/cm^3)	Total Porosity
WIC 7129	12.59	3.02	90.25	717	427	2.254	0.098
WIC 7133	8.71	2.57	54.90	630	434	2.392	0.128
WIC 7135	13.27	4.62	84.63	638	427	2.249	0.101
WIC 7137	10.25	3.18	68.10	665	427	2.343	0.106
WIC 7139	9.36	2.81	64.95	694	428	2.375	0.135
WIC 7142	10.43	3.52	72.37	694	426	2.346	0.122
WIC 7145	10.92	4.18	72.03	660	425	2.331	0.129
WIC 7147	7.28	2.26	47.76	656	434	2.458	0.114
WIC 7151	14.75	5.85	89.61	608	429	2.236	0.105
WIC 7153	7.34	2.45	48.37	659	431	2.489	0.139
WIC 7155	9.67	3.87	69.41	718	429	2.361	0.126
HAR 7038	7.91	3.29	30.17	382	449	2.493	0.031
HAR 7046	6.75	2.93	26.03	386	450	2.526	0.046
HAR 7060	5.78	1.47	19.72	341	447	2.592	0.045
HAR 7070	8.71	2.26	31.27	359	449	2.463	0.035
HAD 7083	7.35	0.75	4.10	56	465	2.589	0.137
HAD 7090	7.41	0.94	4.16	56	464	2.572	0.114
HAD 7094	5.21	0.845	3.52	68	459	2.608	0.121
HAD 7097	5.40	0.75	3.15	58	458	2.609	0.119
HAD 7099	6.51	0.98	3.86	59	463	2.576	0.106
HAD 7101	5.88	0.92	3.1	53	457	2.624	0.118
HAD 7104	5.04	0.72	3.385	67	459	2.620	0.116
HAD 7105	5.85	0.77	3.28	56	461	2.621	0.112

HAD 7110	6.36	1.07	3.79	60	462	2.600	0.094
HAD 7115	6.49	1.12	3.80	59	460	2.614	0.093
HAD 7119	7.15	1.23	3.16	44	459	2.607	0.115

1253

1254

1255 **Table 3.** Rock-Eval evaluation after solvent extraction for four Posidonia samples, wells WIC (0.53%

1256 R_o), HAR (0.89% R_o) and HAD (1.45% R_o).

Sample	S2a (mg/g)	S1 + S2a		S2b (mg/g)	Oil saturation index (mg/gTOC)	Grain density (g/cm^3)	Total porosity (%)	Estimated bitumen content (%)
		(mg/g)	% TOC					
WIC 7129	10.4	13.20	10.5	79.89	104.8	2.236	n.d.	n.d.
HAR 7060	4.5	5.89	10.2	15.25	101.9	2.682	7.8	3.4
HAR 7070	3.5	5.71	6.6	27.79	65.6	2.533	6.3	2.8
HAD 7110	0.7	1.74	2.7	3.05	27.4	2.618	10.1	0.7

1257

1258

1259

1260

Figure 1. Two column

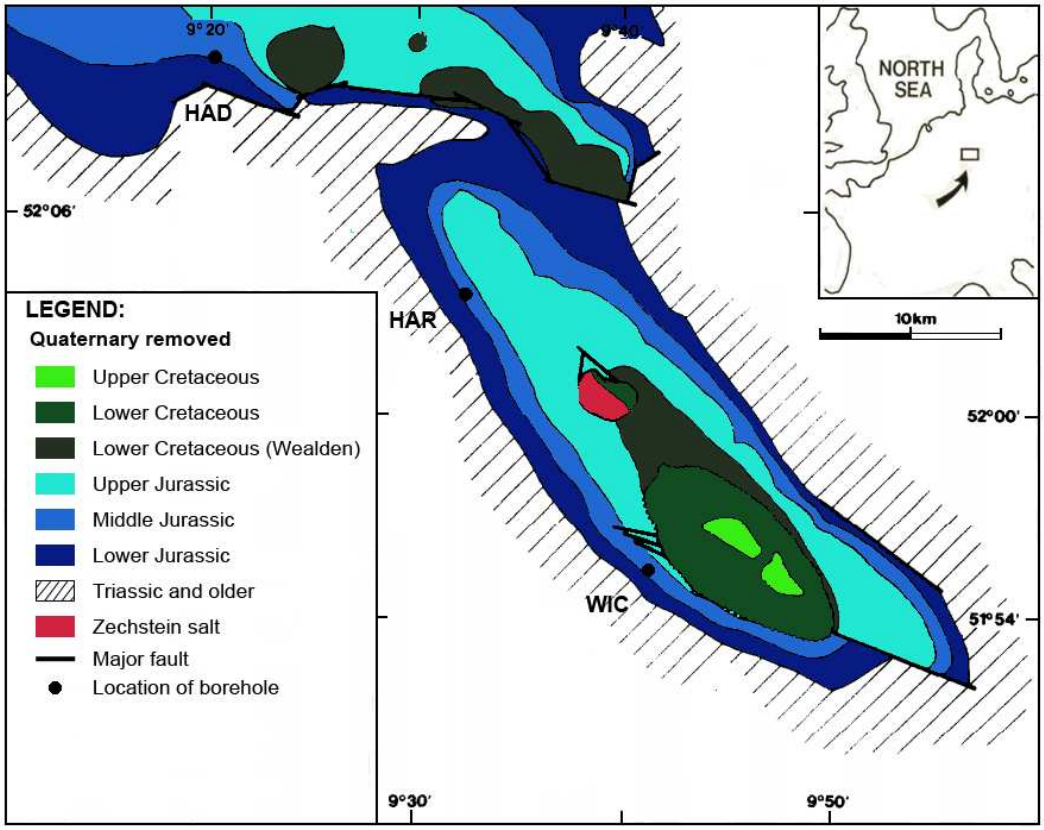

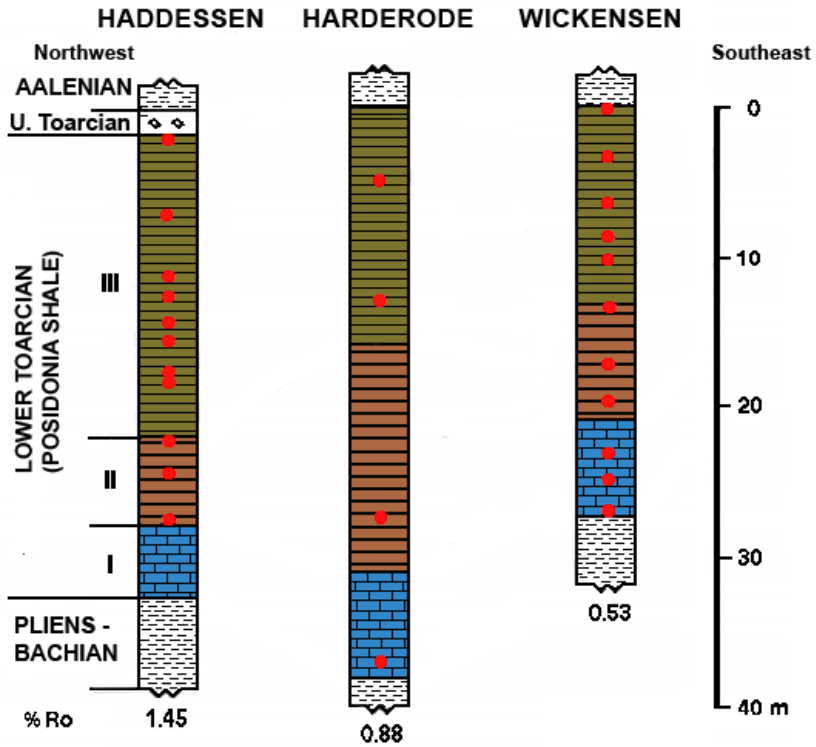

Figure 2 Two column

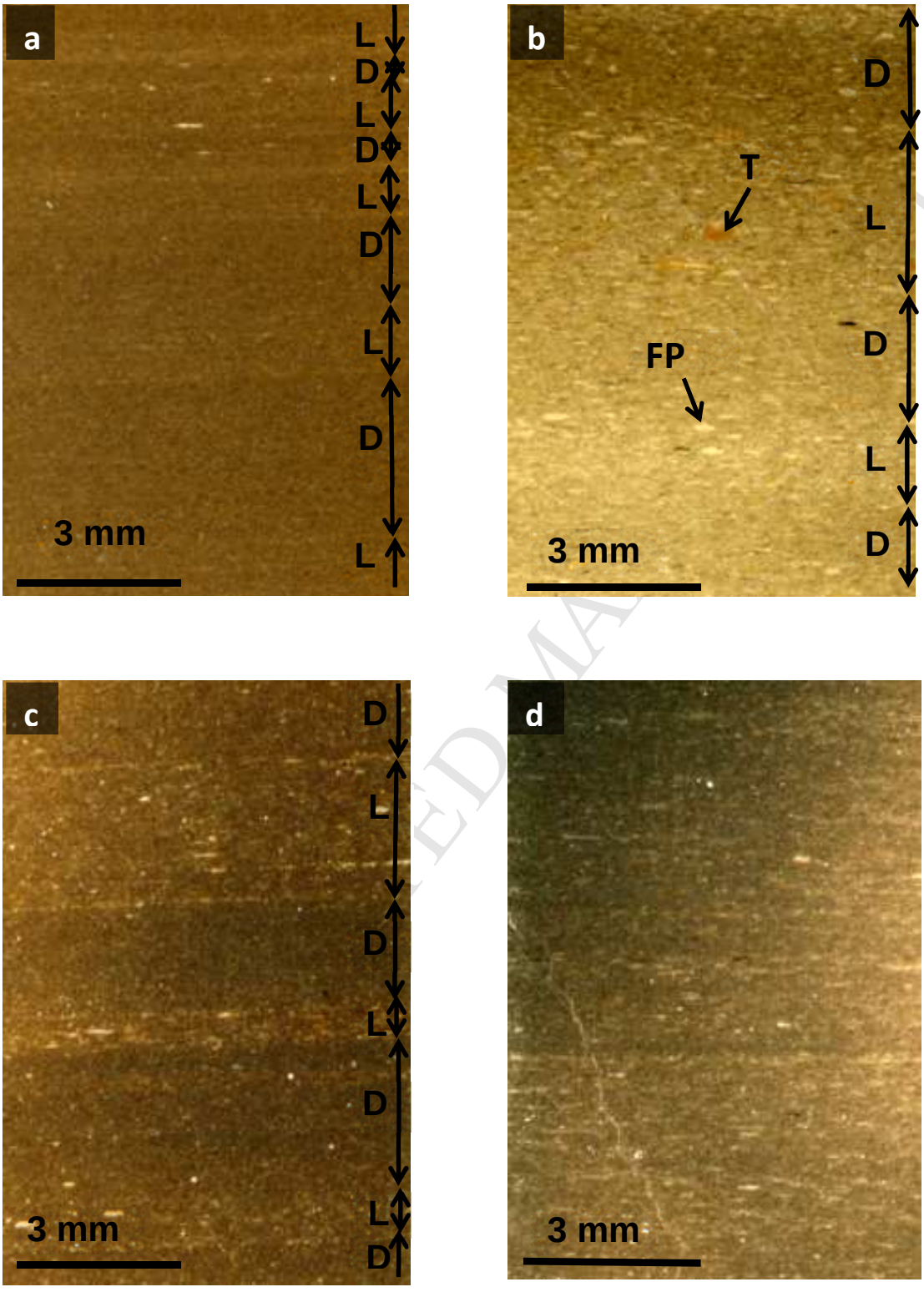

Figure 3 Two column

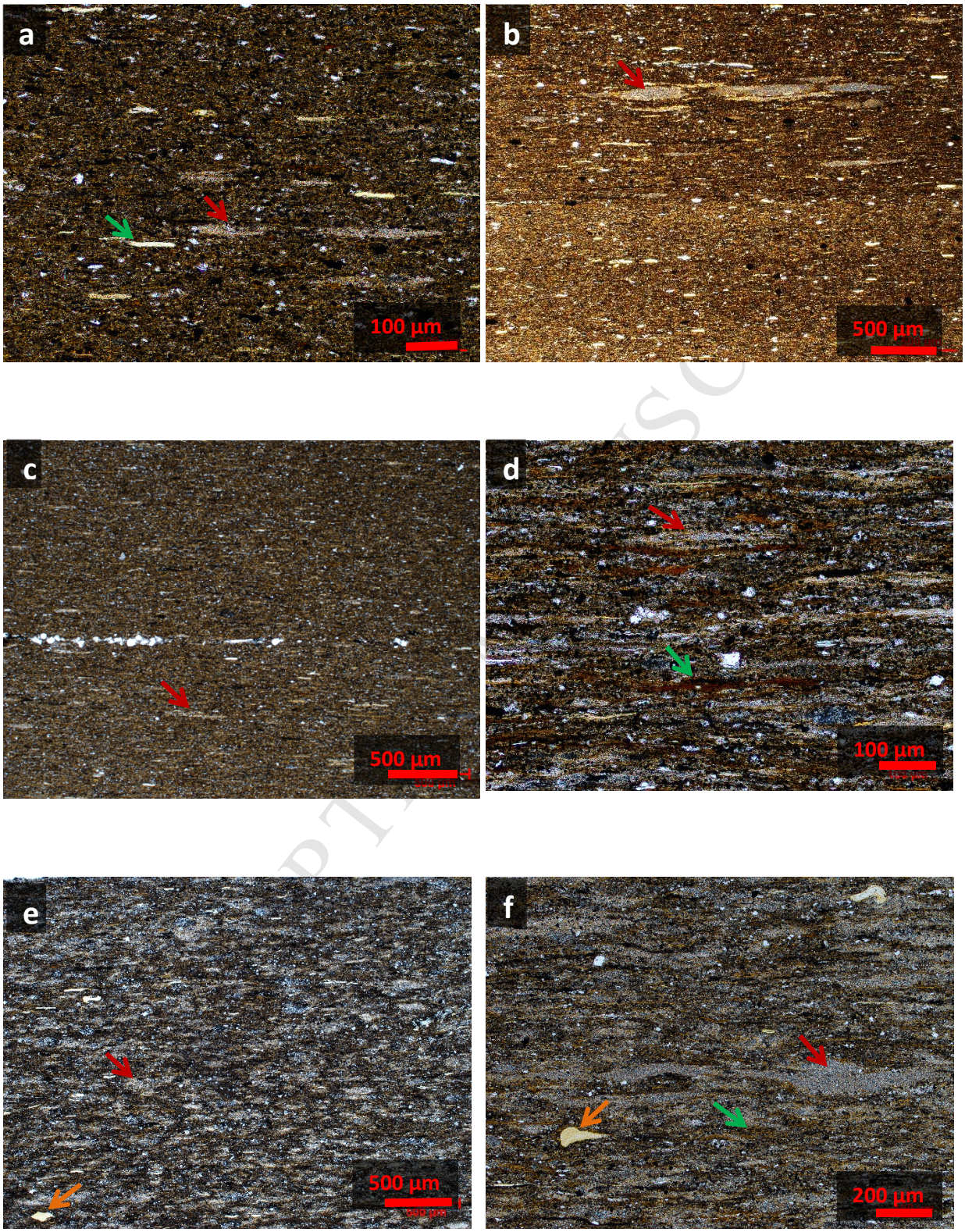

Figure 4 Two column

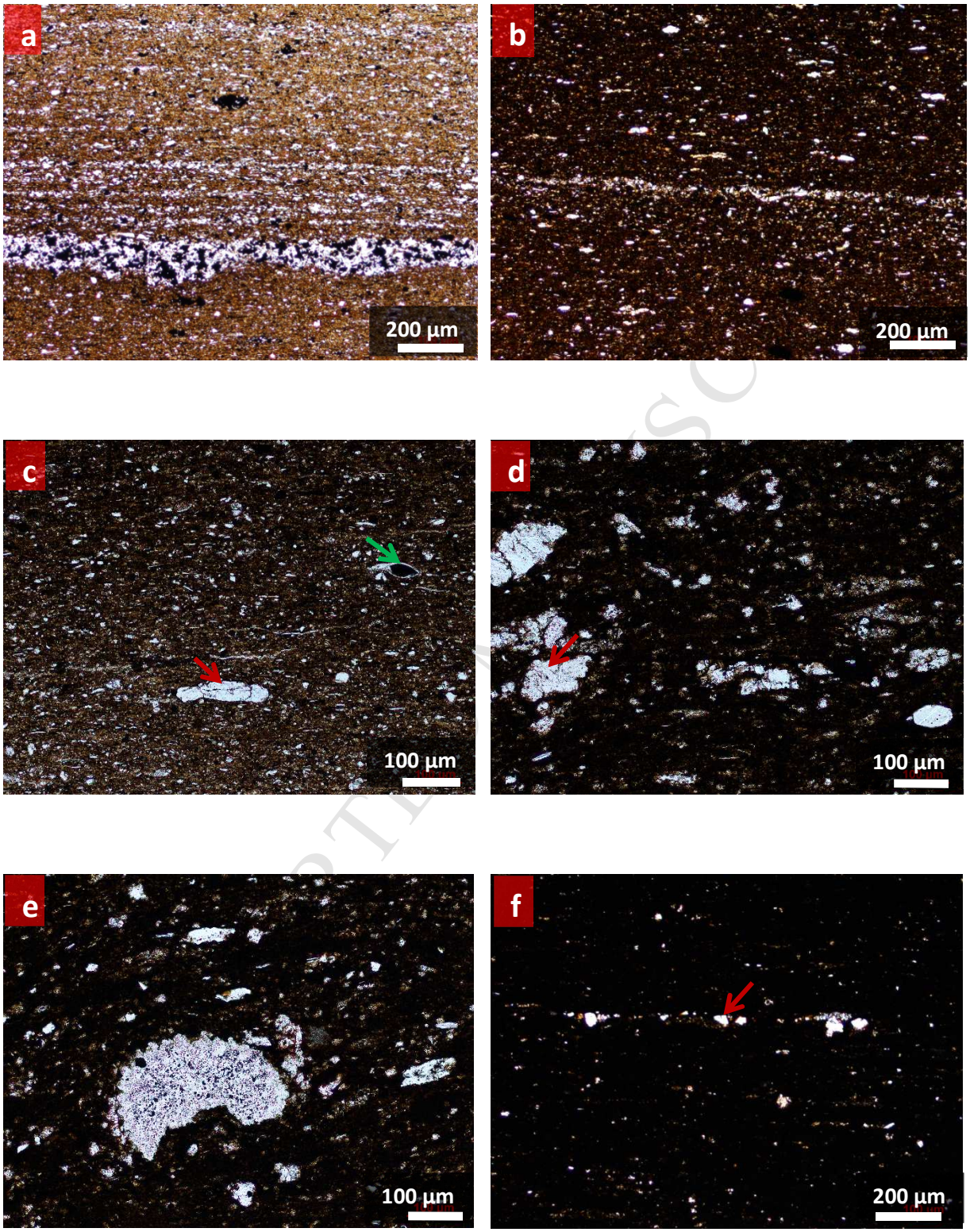

Figure 5 Two column

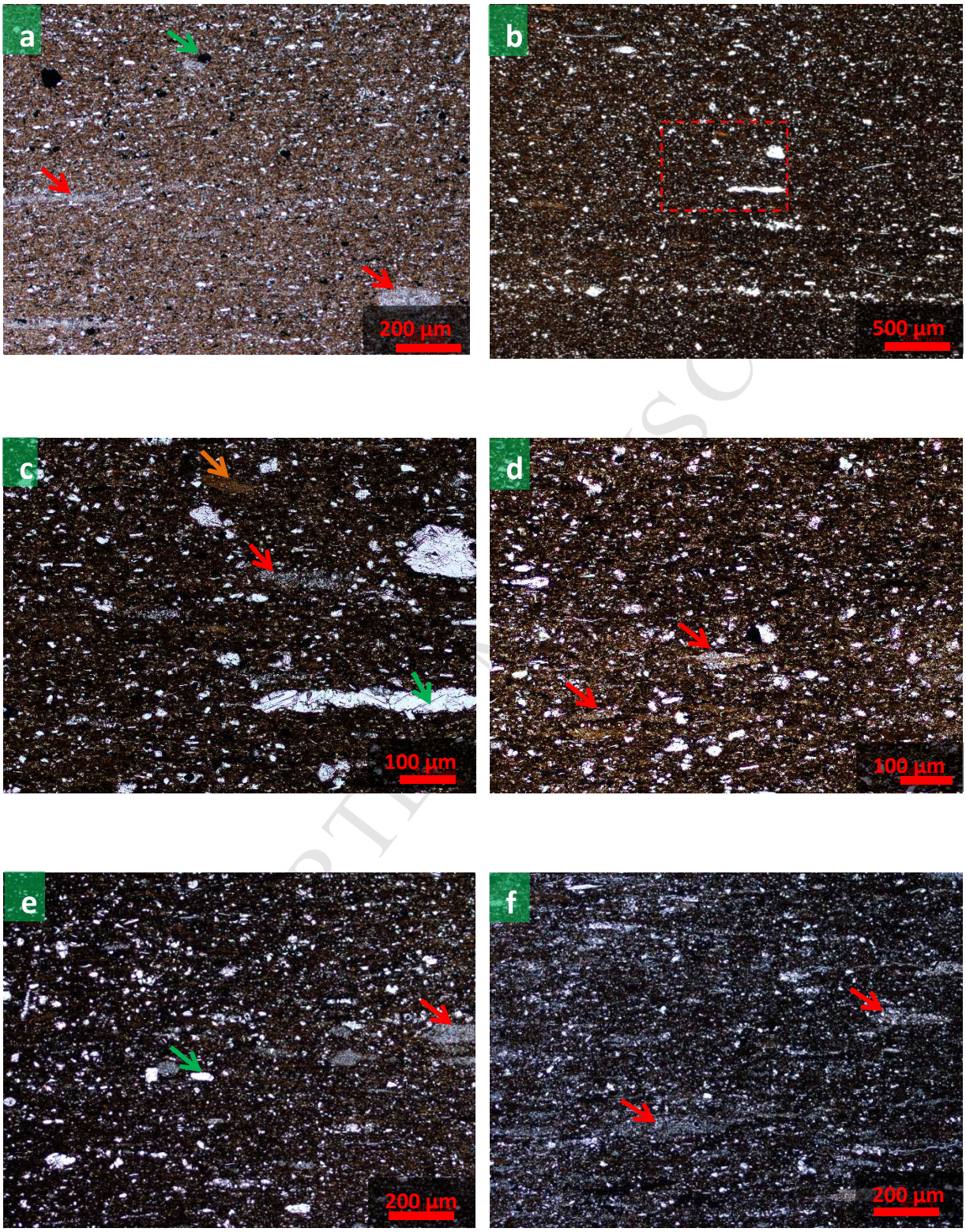

Figure 6 Two column

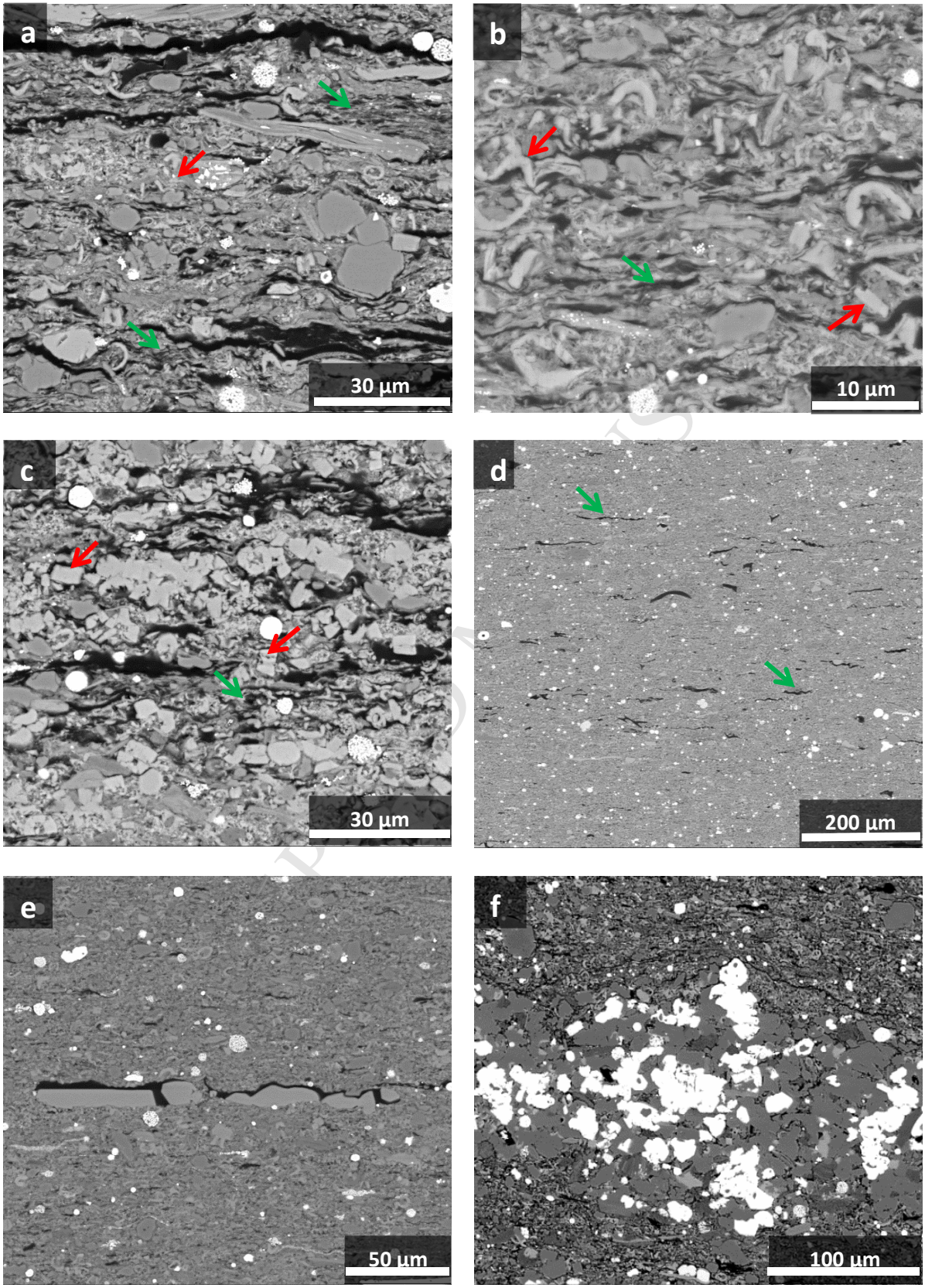

Figure 7 Two column

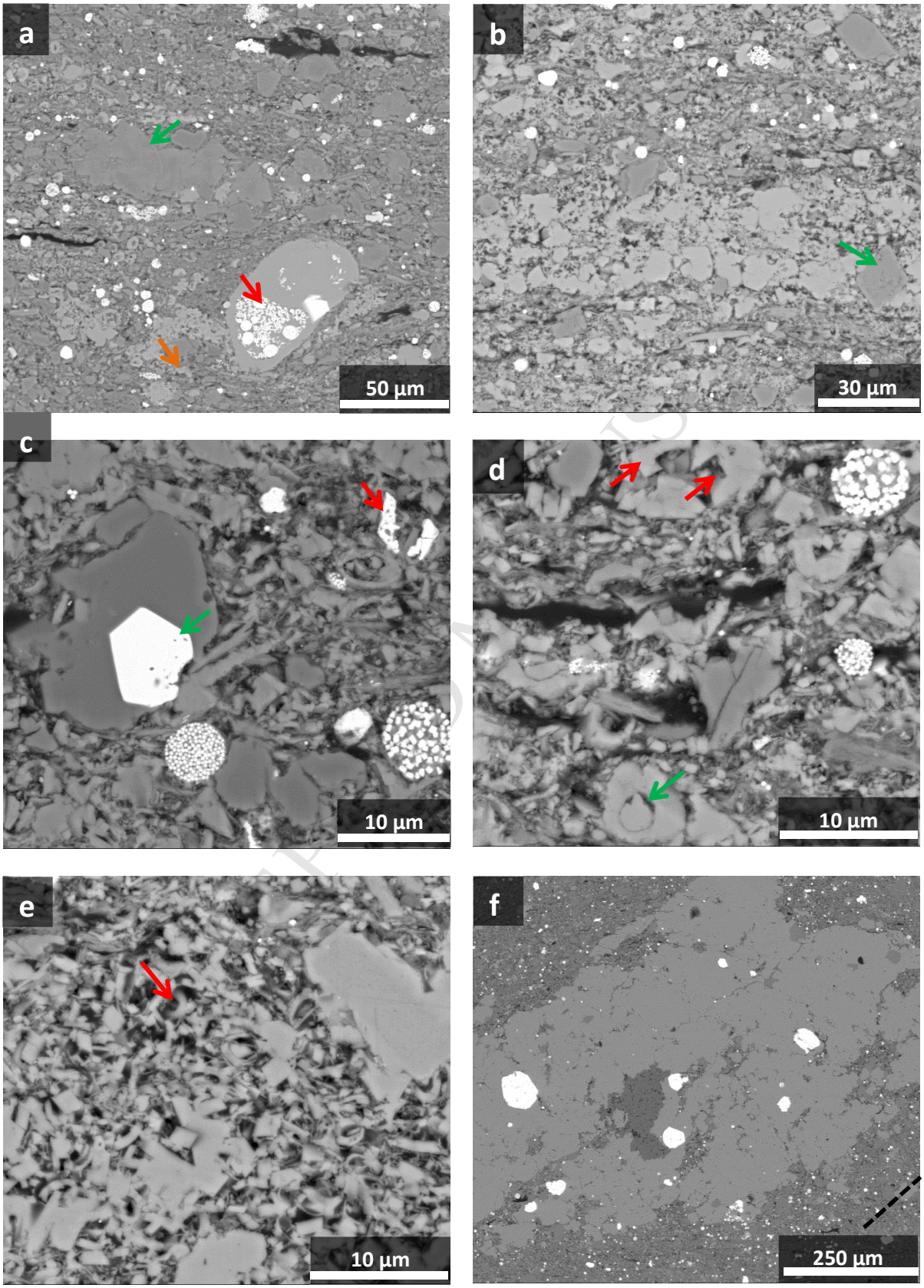

Figure 8 Two column

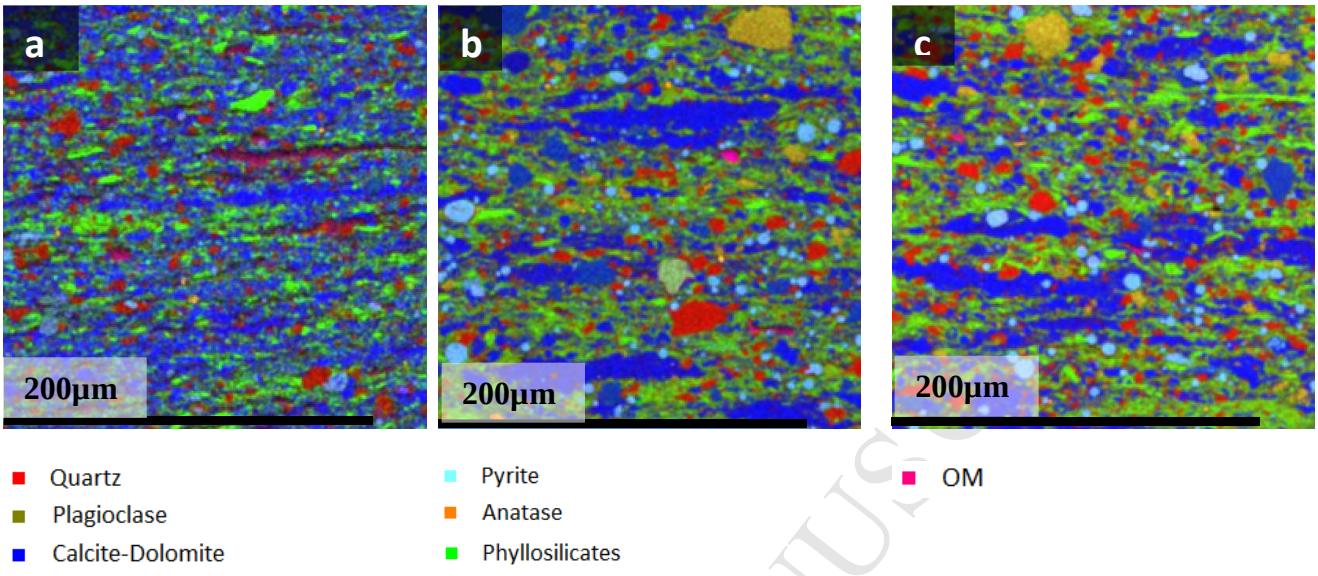

Figure 9 Two column

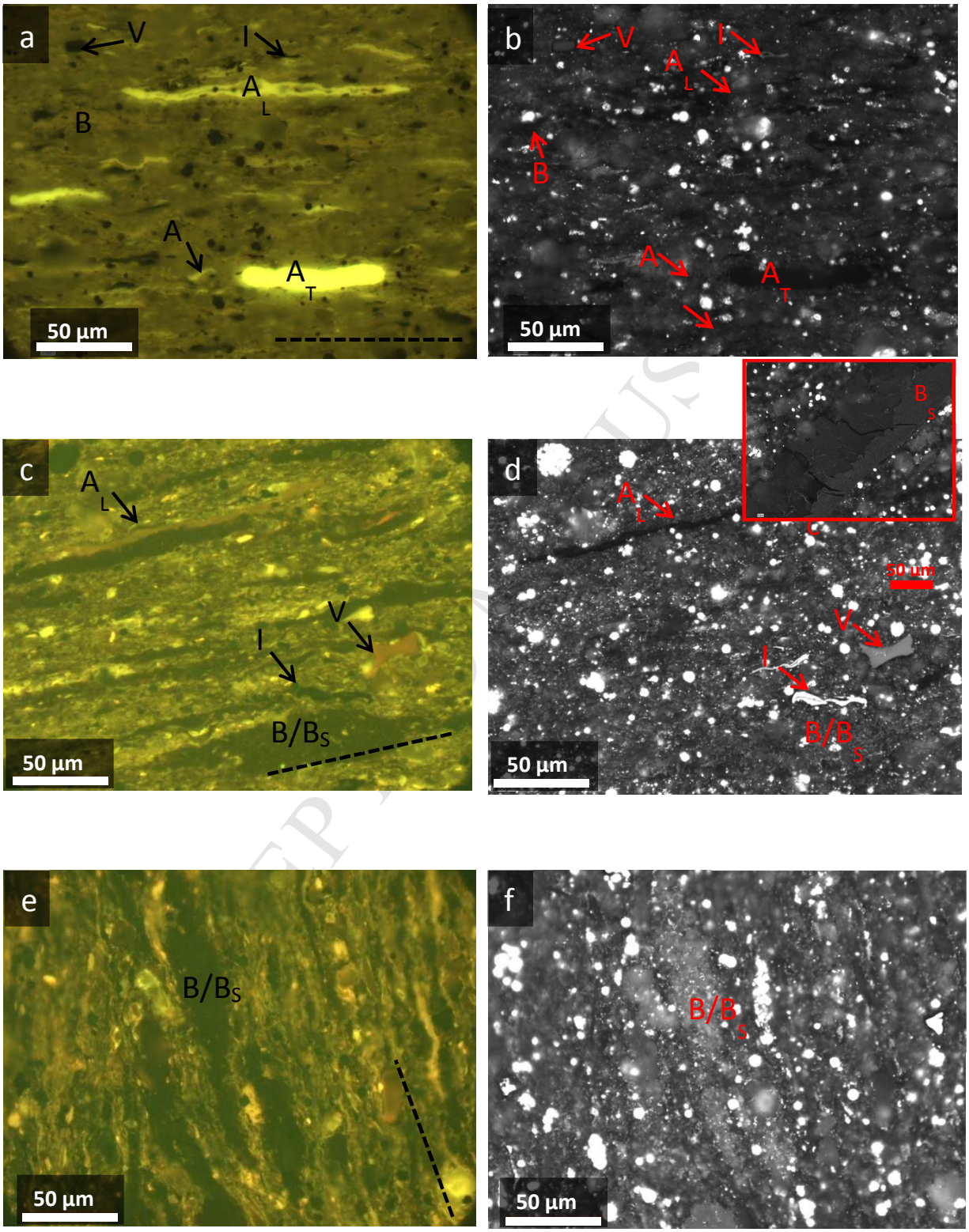

Figure 10 Two column

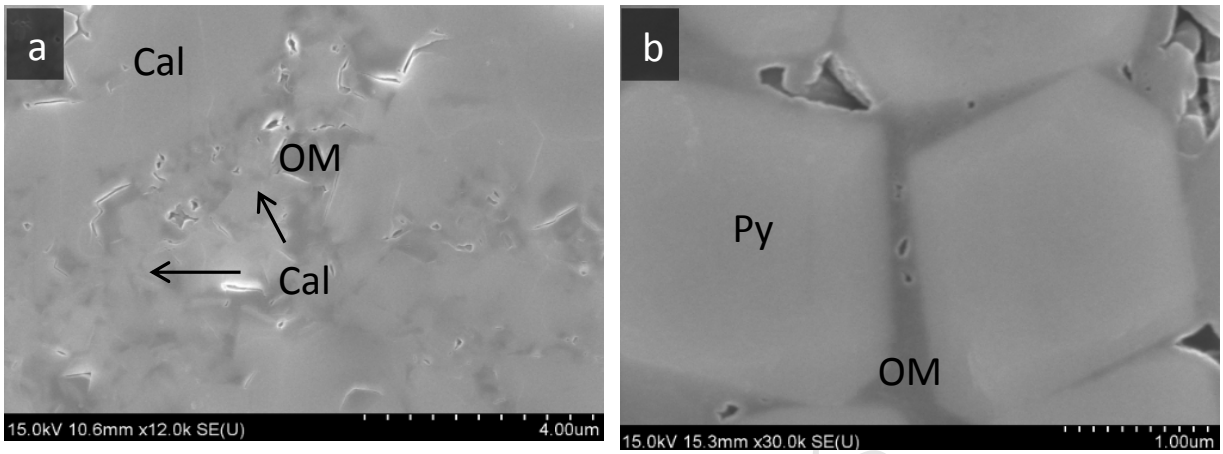

Figure 11 Two column

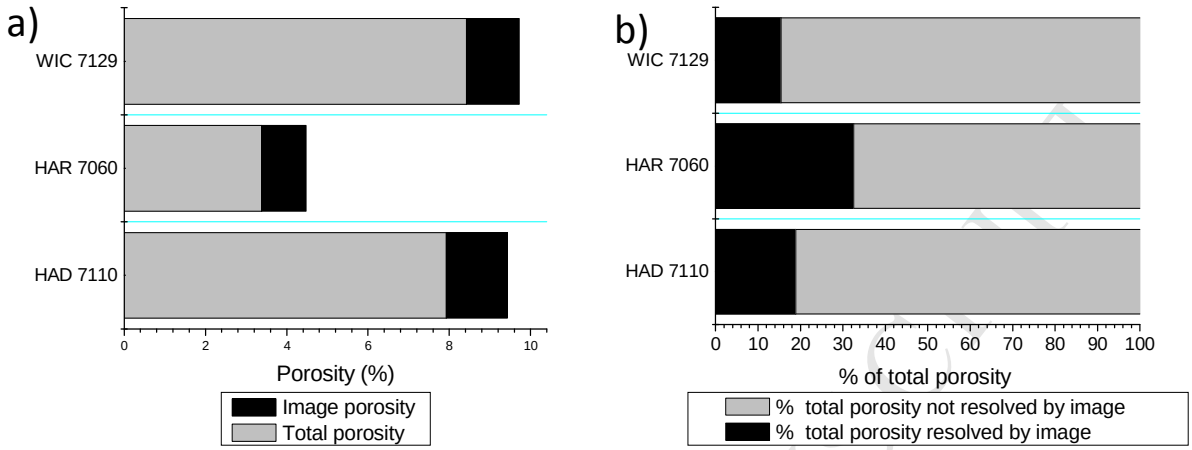

Figure 12 Single column

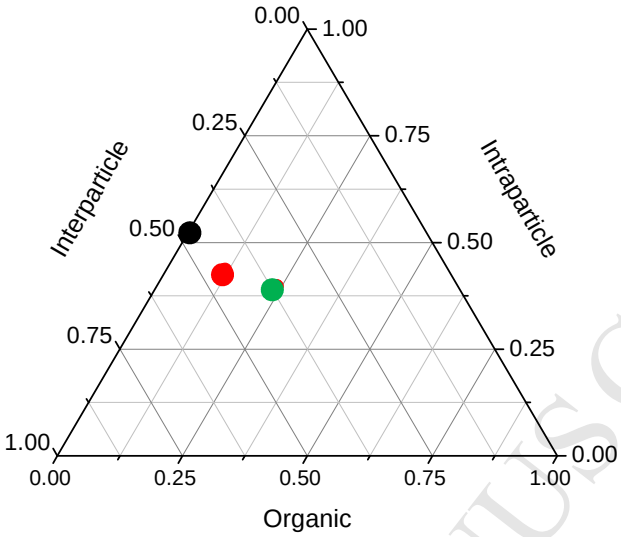

Figure 13 Two column

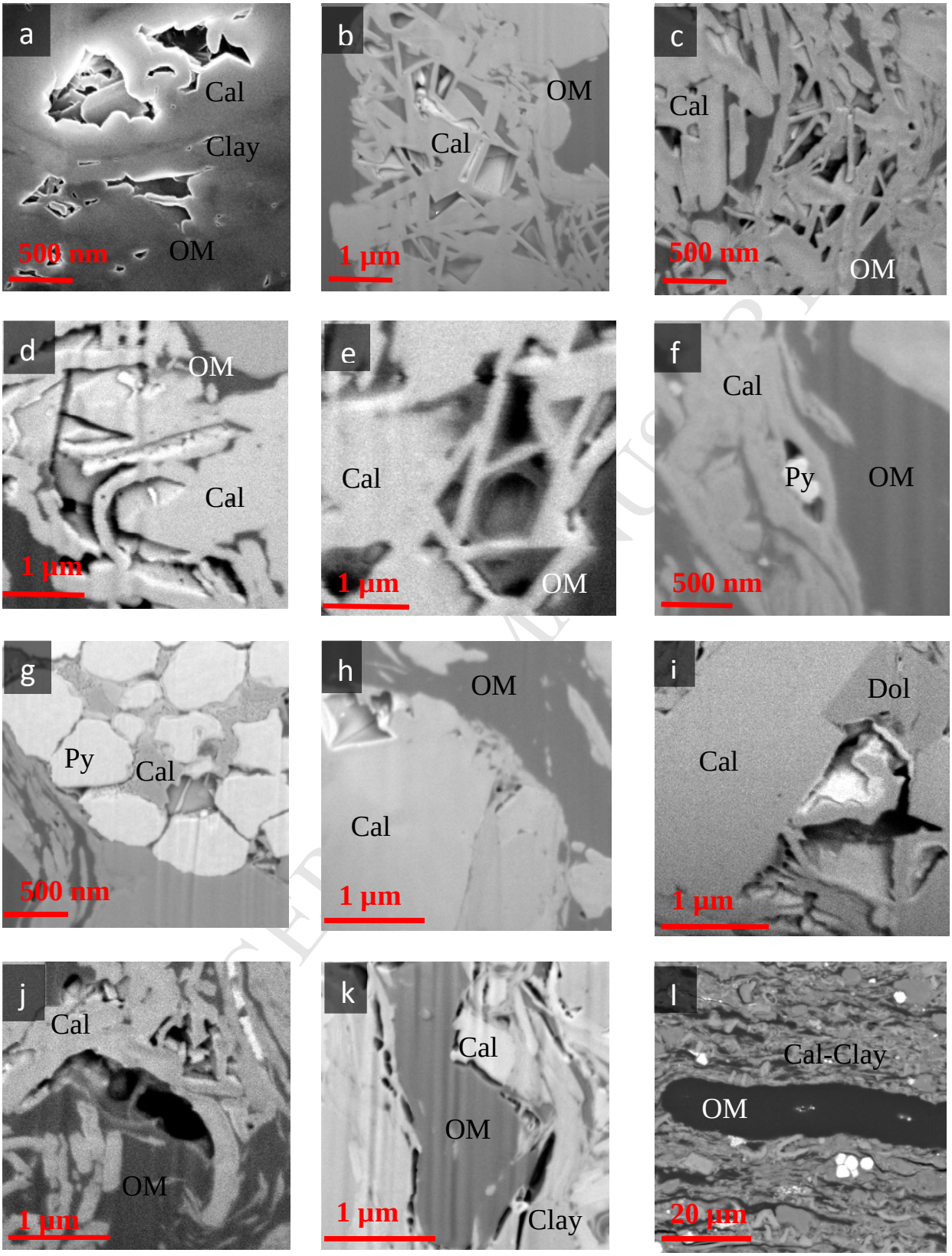

Figure 14 Two column

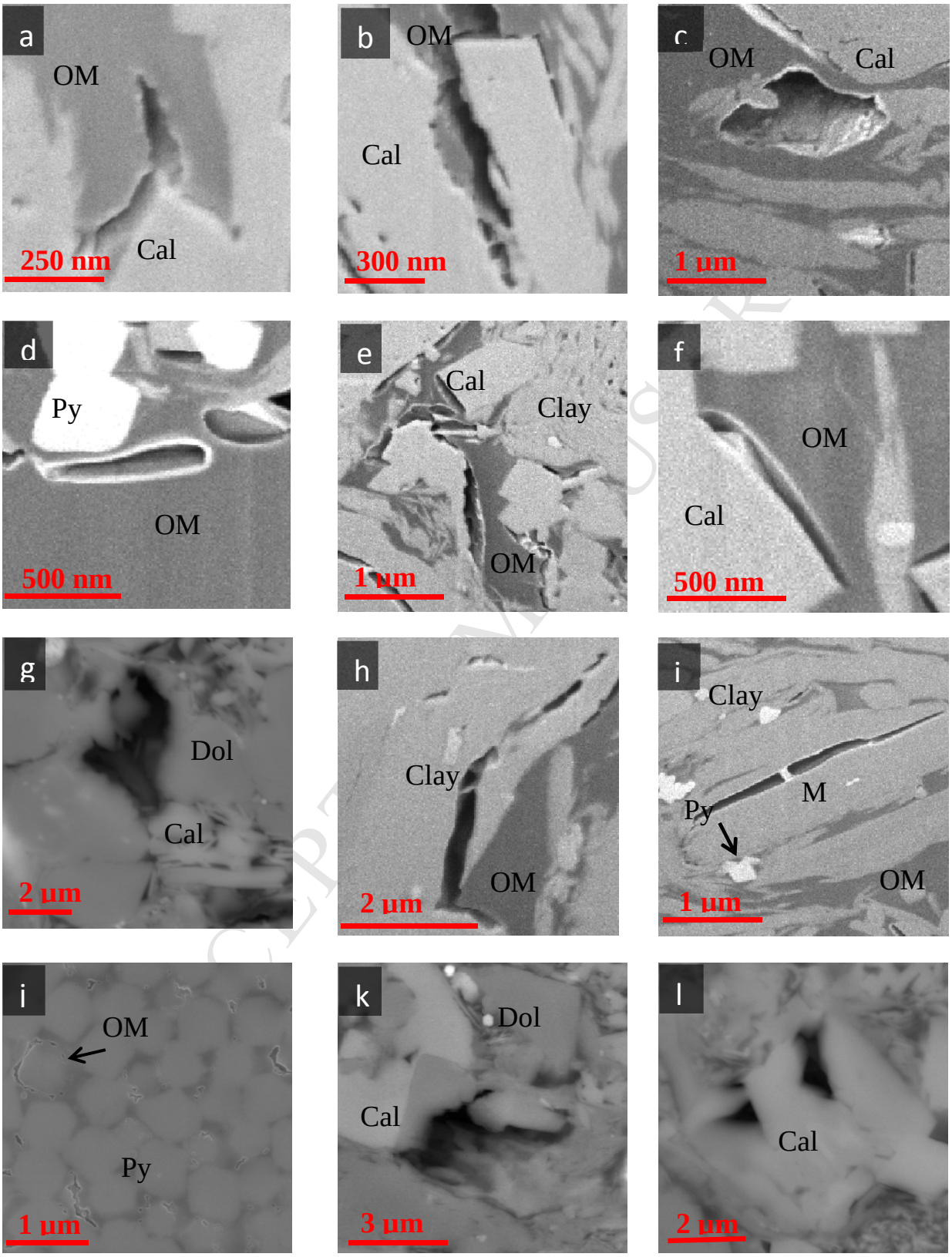

Figure 15 Two column

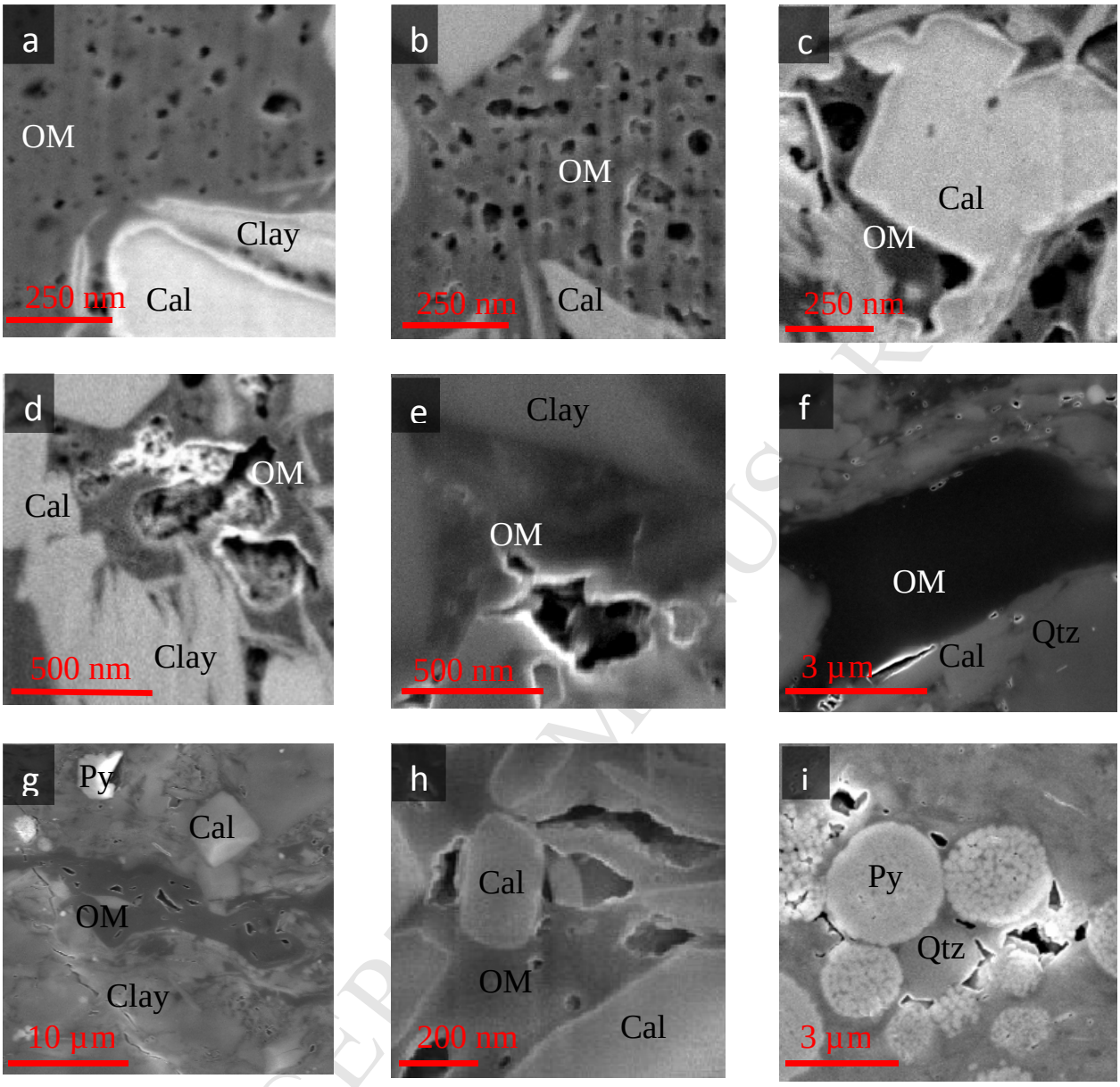

Figure 16 Two column

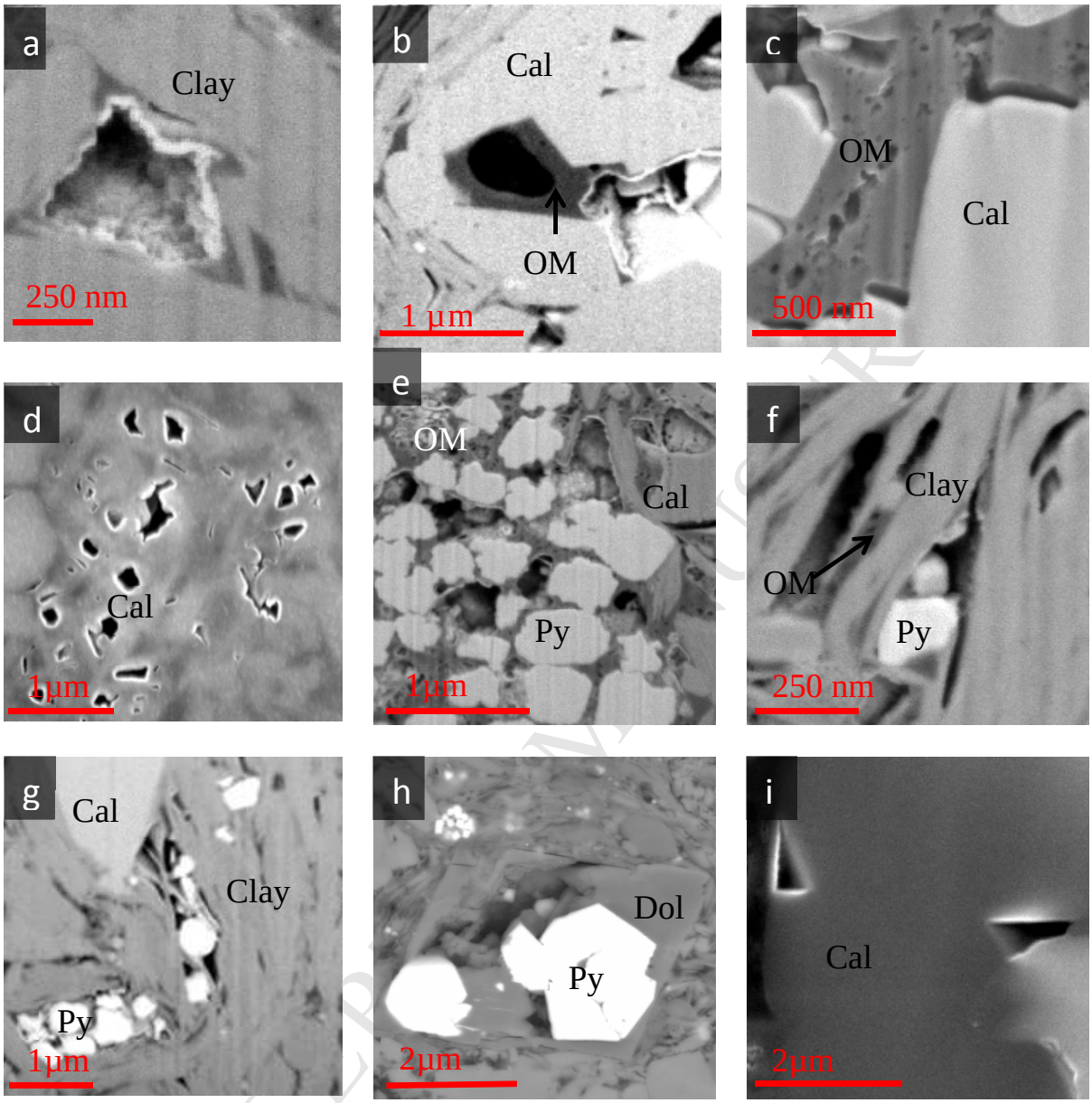

Highlights: Mathia et al. Microscopic, Petrophysical and Geochemical Characterisation of the Lower Toarcian Posidonia Shale: Implications for Porosity Evolution in an Organic-rich, Calcareous Shale

Porosity of organic-rich, calcareous Posidonia Shale halves in oil window and doubles in gas window

Porosity changes driven by carbonate diagenesis and retention/gasification of bitumen

Pores quantifiable by SEM (> ca. 50 nm) only account for 14-25% of total porosity

Macroporosity of single organic particles in gas window range from 0-40%

Much of porosity generated in gas window is in micro- and mesopores